UNIVERSITY
OF OSLO

Master's thesis

A Quantitative Study of the Gradient Drift Instability in Polar Cap Patches and their Interhemispheric Occurrence Rate

Kristoffer Falk Austnes

Plasma and Space Physics
30 ECTS study points

Department of Physics
Faculty of Mathematics and Natural Sciences

Spring 2023

Kristoffer Falk Austnes

A Quantitative Study of the Gradient Drift Instability in Polar Cap Patches and their Interhemispheric Occurrence Rate

Supervisor:
Lasse B. N. Clausen

Abstract

In this master thesis we will study a space weather phenomena known as polar cap patches (PCPs). Polar cap patches are patches of high density plasma drifting anti-sunward across the polar cap. As a result of this anti-sunward drift, the patches have a leading and a trailing edge. We will investigate whether the gradient drift instability (GDI) results in more complex plasma density structuring in the trailing edge of polar cap patches. This is done by the processing and analyzing of in situ measurements of the ionospheric plasma density made by the Swarm satellite constellation. The collected data span over a 5.5 year period, from July 2014 to the end of 2019. Subsequently, we compared the density structures in the trailing and leading edge of polar cap patches using the standard deviation of linear regressions with respect to the plasma density. Statistical analysis of the standard deviation ratios was done using a combination of histograms and bar charts. The results of this study suggest that there is in fact a substantial difference in density structuring in polar cap patch edges. The underlying hypothesis, stating that the gradient drift instability affects the trailing edge of polar cap patches, is therefore strengthened.

Based on this, we will also investigate when we can expect signal degrading due to the formation of complex density structures in polar cap patches to be most prevailing. Therefore, we have conducted an interhemispheric polar cap patch occurrence rate study. The results of this study present that polar cap patches occur more frequently during local winter conditions, with respect to both hemispheres. Ultimately, suggesting that signal degrading is prominent during local winter conditions.

Acknowledgements

I would like to express my deepest appreciation to my supervisor Lasse B. N. Clausen. You have provided me with guidance and support throughout the process of writing this master thesis. Additionally, your unprecedented pedagogical skills have assisted me in achieving a better understanding of different aspects of space physics and space weather.

I am also grateful to all of the fantastic people at the Plasma and Space Physics department. You have welcomed my fellow master students and I with open arms. The occasional joint grill-lunch and the monthly space-waffles Friday are dear memories.

Lastly, I would like to thank my friends and family for their unwavering support throughout my plasma and space physics adventure. This would not have been possible without you.

Contents

List of Figures

List of Tables

Chapter 1

Introduction

We are inclined to become more dependent on the reliability of different Global Navigation Satellite System (GNSS) signals due to the constant development of technology in the modern society. GNSS signal quality is especially important in the polar regions as these regions predominantly depend on positional and communication data from satellites rather than ground based instruments. GNSS signals propagating through the Earth's ionosphere are susceptible to rapid fluctuations in both phase and amplitude due to changes in the medium's refractive index. This is known as scintillation. Space weather phenomena resulting in large changes in ionospheric plasma density can be especially harmful for GNSS signal quality, given that the refractive index is largely dependent on the electron density.

Polar cap patches (PCPs) are a space weather phenomena occurring in the Earth's ionosphere as a result of the interaction between the Earth's magnetic field and the interplanetary magnetic field travelling through space with the solar wind. This interaction takes place on the dayside and nightside of the Earth and is known as magnetic reconnection. Dayside magnetic reconnection results in high density plasma drifting anti-sunward across the polar cap regions. Thus, causing significant degradation of GNSS signal quality. Polar cap patches and the gradient drift instability (GDI) is therefore of particular interest in a space weather setting.

Polar cap patches have been the subject of interest in multiple case studies and research letters. However, the relation between polar cap patches and the gradient drift instability has not been investigated as often. Spicher et al. have investigated the gradient drift instability growth time in polar cap patches (Spicher et al. 2015). The study used Swarm data from a single day, 29 December 2013, in order to compare a dayside PCP with a nightside PCP. They successfully calculated GDI growth times and found out that internal kilometer-scale structures persist as the polar cap patches drift across the polar cap. This could further confirm the preexisting view that GDI can cause density structuring in the trailing edge of polar cap patches.

Studies done by Chartier et al. 2018 and Spicher et al. 2017 have taken a closer look at the annual occurrence rate of polar cap patches in the northern and southern hemisphere. Both studies take advantage of Swarm data. However, the studies arrive at somewhat contradictive conclusions. Spicher et al. conclude that the polar cap patch occurrence rate is highest during local winter conditions. On the contrary, Chartier et al. conclude that PCP's occur more frequently around December for both hemispheres.

The Swarm constellation had barely started its mission at the time of the previously mentioned studies, this is especially true with respect to the PCP GDI study (Spicher et al. 2015). The Swarm constellation have now been collecting data for almost a decade, providing an unprecedented opportunity for a quantitative polar cap patch gradient drift instability study at a larger scale. This is what inspired the idea for this master thesis. The hypothesis is that polar cap patches drifting across the polar cap regions are affected by the gradient drift instability. In other words, that the gradient drift instability produce complex plasma density structures in the trailing edge of polar cap patches.

A secondary objective of this master thesis is to investigate when we can expect polar cap patches to most frequently affect the signal quality of GNSS signals. This is done though studying the polar cap patch occurrence rate in the northern and southern hemisphere. The goal is to illuminate whether the polar cap patch occurrence rate correlate to the preexisting underlying physical theories - stating that the occurrence rate is highest during local winter conditions.

Chapter 2

Theory

The following chapter aims to provide the theoretical background necessary to understand the underlying physics and discussions made in this master thesis.

Beginning with the definition of a plasma we move into fundamental plasma physics before describing the different plasma models; single particle motion, kinetic theory and magnetohydrodynamics (MHD). Essential aspects of the solar wind and its interaction with the Earth's magnetic field - the frozen in theorem and magnetic reconnection - are explained. We then take a closer look at our solar system's largest plasma source, the Sun, and subsequently explain the solar wind and the interplanetary magnetic field. Additionally, the dynamics of the Earth's magnetosphere and ionosphere are presented through solar impact and the ever so important Dungey cycle. Lastly we visit the core aspects of this thesis; space weather effects (polar cap patches), the gradient drift instability (GDI) and scintillation.

2.1 Plasma Physics

In addition to solid, liquid and gas, plasma is known as the fourth state of matter. Plasma is defined as "a quasineutral gas of charged and neutral particles which exhibits collective behavior" (Chen 2016, p. 2). Quasineutrality means that there is an equal amount of ions and electrons, $n_i = n_e$ (Pécseli 2020). Given that the number of positively charged ions is equal to the number of negatively charged electrons the plasma has to have a net charge of zero, due to it being quasineutral. In plasma physics there are three common ways to describe the behaviour of a plasma: single particle motion, magnetohydrodynamics (MHD) and kinetic theory. In the following paragraphs I will introduce the core aspects of single particle motion in order to describe the application of magnetohydrodynamics on plasma.

2.1.1 Single Particle Motion

Single particle motion is a simplified plasma model that is often used to describe the trajectories of individual particles only. Single particle motion disregards the collective behaviour of the plasma (Pécseli 2020). Due to the fact that plasma consists of charged particles, their motion can be described using three well known equations. By applying Newton's 2nd law, $\Sigma \boldsymbol{F} = m\boldsymbol{a}$, the Coulomb force, $\boldsymbol{F}_C = q\boldsymbol{E}$, and the Lorentz force, $\boldsymbol{F}_L = q(\boldsymbol{v} \times \boldsymbol{B})$, we can derive the equation of motion (EOM) for a single charged

particle. The equation of motion is given by

$$\boldsymbol{F} = q(\boldsymbol{E} + \boldsymbol{v} \times \boldsymbol{B}) \tag{2.1}$$

where $\boldsymbol{F}$ is the force which results in acceleration (Lorentz force), q is the charge of a given particle, $\boldsymbol{E}$ is the electric field, $\boldsymbol{v}$ is the velocity of the particle and $\boldsymbol{B}$ is the magnetic field. This equation of motion says that a given particle with charge q moving through an electric and magnetic field with the velocity $\boldsymbol{v}$ experiences a force, which changes the particles' trajectory (Russel et al. 2016).

Given that the particle density is low in single particle motion, the magnetic and electric fields that are induced by the presence of charged particles can be neglected when compared to the preexisting external fields (Pécseli 2020). An electrically charged particle travelling through a uniform magnetic field will gyrate, meaning that it will follow a circular trajectory around a guiding center. This is due to the perpendicular magnetic force. When introducing an electric field the particle is affected by the Lorentz force (equation 2.1). Including a non-zero force $\vec{F}_{\perp}$, e.g. an electric field, the charged particles will be accelerated. As the particle moves it starts to gyrate due to the magnetic field. Eventually, the gyrating particle will move against the external force causing it to decelerate and stop away from the starting position. This positional shift is known as drift. Different variations of drift are shown in figure 2.1.

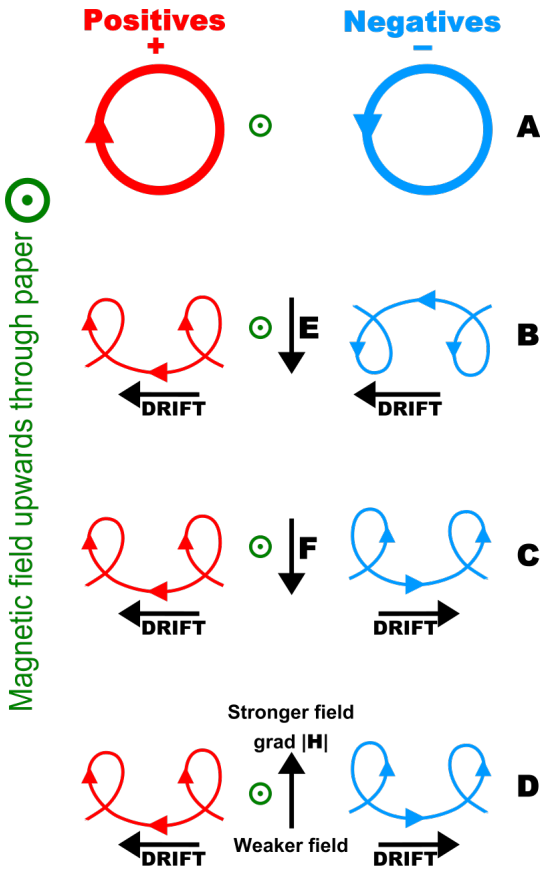

Figure 2.1: Illustration of particle gyration and different variations of drift.
https://www.plasma-universe.com/charged-particle-drift/

2.1.2 Plasma Parameters

Magnetohydrodynamics (MHD) is established as a useful tool when modelling large scale plasma as a fluid in space physics. MHD is applied when the characteristic time and scale of the fluid is much greater than the plasma period and Debye length, respectively (Pécseli 2020). When describing a plasma it is therefore important to take different parameters into account. These parameters are called plasma parameters.

Consider an electrically neutral plasma, made up of positively charged ions and negatively charged electrons. Displacing the electrons with respect to the ions result in an oscillating motion due to the Coulomb force - which pulls the electrons back toward the ions. The ions are considered to be stationary when compared to the electrons, given that $m_i >> m_e$. Subsequently, the electrons will oscillate at the plasma frequency given by

$$\omega_{pe} = \sqrt{\frac{e^2 n_e}{\epsilon_0 m_e}} \tag{2.2}$$

where e is the elementary electric charge, n_e is the electron density, ϵ_0 is the vacuum permittivity and m_e is the electron mass. The plasma period is the characteristic plasma time and is given by

$$\tau_p = \frac{2\pi}{\omega_{pe}} \tag{2.3}$$

where ω_{pe} is the plasma frequency as seen in equation 2.2 (Pécseli 2020). The characteristic length of a plasma known as the Debye length (Chen 2016; Pécseli 2020; Russel et al. 2016), is given by

$$\lambda_D = \sqrt{\frac{\epsilon_0 k_B T}{e^2 n}} \tag{2.4}$$

where k_B is the Boltzmann constant, T is the temperature and n is the particle density. The Debye length can be considered as "the distance traveled by a plasma particle within one appropriate plasma period" (Pécseli 2020, p. 138).

In addition to the plasma period and the Debye length there is another important plasma parameter used for classifying plasmas; the plasma beta (Pécseli 2020). The plasma beta, β, is defined as the ratio between the thermal plasma pressure and the magnetic pressure (Pécseli 2020; Chen 2016) and is given by

$$\beta = \frac{n\kappa T}{B^2/2\mu_0} = \frac{\text{Particle pressure}}{\text{Magnetic field pressure}} \tag{2.5}$$

By taking the plasma beta, β, into account the dominating forces in a plasma can be identified. Plasmas with high β are dominated by kinetic forces, and low β plasmas are dominated by magnetic forces.

2.1.3 Magnetohydrodynamics (MHD)

As previously mentioned the internally induced magnetic and electric field in a plasma are negligible in single particle motion. However, these fields can not be ignored for a plasma consisting of a large number of particles. This is due to the fact that a single charged particle can interact with a multitude of other charged particles simultaneously through the long range of the Coulomb force (Pécseli 2020). The collective effects of the plasma particles have to be taken into account.

This is achieved using the kinetic theory. The distribution of particle velocities are assumed to be Maxwellian in kinetic theory, making it possible to identify the space, time and velocity of any given particle in a plasma (Pécseli 2020). In principle the plasma could then be described by tracing each individual particle. However, this is extremely computationally heavy and can only be done for small plasma volumes (Russel et al. 2016). As an alternative a fluid description of a bulk plasma is found using hydrodynamics. This is called magnetohydrodynamics (MHD).

MHD equations

When dealing with incompressible, ideal MHD, the equations describing the MHD are derived using the equation of motion (2.1) in addition to Maxwell's equations for

magnetised plasma (Russel et al. 2016; Pécseli 2020). The resulting MHD equations are given as (Pécseli 2020, p. 188)

$$\frac{\partial}{\partial t}\boldsymbol{B} = \nabla \times (\boldsymbol{u} \times \boldsymbol{B}) \tag{2.6}$$

$$\frac{\partial}{\partial t}\rho + \boldsymbol{u} \cdot \nabla\rho = 0 \tag{2.7}$$

$$\nabla \cdot \boldsymbol{u} = 0 \tag{2.8}$$

$$\rho\left(\frac{\partial}{\partial t}\boldsymbol{u} + \boldsymbol{u} \cdot \nabla\boldsymbol{u}\right) = -\nabla p + \frac{1}{\mu_0}(\nabla \times \boldsymbol{B}) \times \boldsymbol{B} \tag{2.9}$$

In the equations above $\boldsymbol{B}$ is the magnetic field, $\boldsymbol{u}$ is the bulk velocity of the plasma, ρ is the plasma density, p is the plasma pressure and μ_0 is the vacuum permeability constant. The equations above are commonly known as Faraday's law (2.6), the continuity equation (2.7), equation for incompressibility (2.8) and the momentum equation (2.9). Faraday's law (2.6) connects the magnetic and electric field, and is often found on the form

$$\nabla \times \boldsymbol{E} = -\frac{\partial \boldsymbol{B}}{\partial t} \tag{2.10}$$

In order to derive equation 2.6 we can insert Ohm's law under ideal MHD conditions, meaning the conductivity of our plasma tends to infinity ($\sigma \to \infty$). This results in

$$\boldsymbol{J} = \boldsymbol{\sigma}(\boldsymbol{E} + \boldsymbol{u} \times \boldsymbol{B}) \underset{\sigma\to\infty}{\Rightarrow} \boldsymbol{E} = -\boldsymbol{u} \times \boldsymbol{B} \tag{2.11}$$

When inserting Ohm's law (2.11) into Faraday's law (2.10), we have eliminated the dependency of the electric field, $\boldsymbol{E}$. We have now obtained Faraday's law for ideal MHD, as shown in equation 2.6.

The physical meaning of the continuity equation (2.7) is that there are no sources or sinks of particles in the MHD system. In other words, no particles are added, created or lost (Pécseli 2020). This adds an important element to our MHD system - it is possible to reverse the system in time.

When modelling plasma using the MHD equations we need to make some simple assumptions. We assume plasma can be characterized as a single fluid. Thereby suggesting that the ions and electrons of the plasma behave as one medium, characterized by a large conductivity (Pécseli 2020; Chen 2016).

2.1.4 Frozen in Theorem

The frozen in theorem is a very important aspect when working with plasma physics, and needs to be considered for ideal MHD. For ideal MHD the conductivity of the plasma tends to infinity, $\sigma \to \infty$ (Pécseli 2020). When the frozen in theorem is valid the magnetic field lines are considered to be *frozen* into the conducting fluid (Russel et al. 2016). The frozen in theorem states that the magnetic flux through a delimited area remains constant as the area moves with the fluid. Additionally, any magnetic field line connecting two fluid elements will remain connected to these elements (Russel et al. 2016). When dealing with plasmas where the conductivity tends to infinity it is therefore possible to identify the motion of the magnetic field lines through the motion of particles in space (Pécseli 2020; Russel et al. 2016). However, this is not always the case. The frozen in theorem does not hold for resistive, non-ideal MHD (Pécseli 2020).

2.1.5 Magnetic Reconnection

Given that this master project investigates a phenomena - polar cap patches - resulting from the coupling between the Earth's magnetic field and interplanetary magnetic field, it is essential to understand the primary process that is known as magnetic reconnection (Russel et al. 2016). Magnetic reconnection occurs when anti-parallel magnetic field lines are pushed together by external forces, as illustrated in figure 2.2. This reconnection is what generates the dynamic coupling of the Earth's magnetic field and the interplanetary magnetic field (IMF) (Russel et al. 2016), allowing plasma flowing in interplanetary space to find its way into the Earth's magnetosphere and ionosphere.

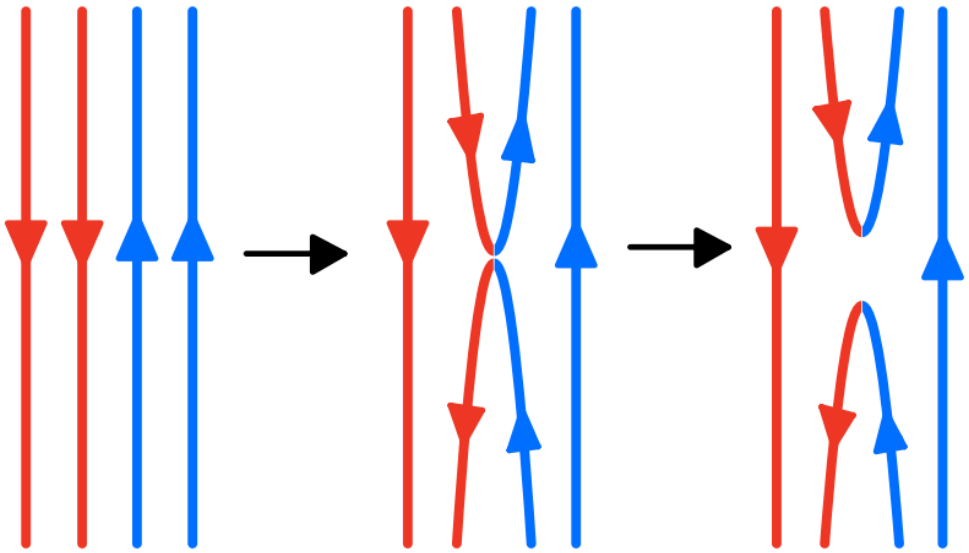

Figure 2.2: Illustration of magnetic reconnection. The colors represent different magnetic regions. Red and blue arrows indicate the direction of the magnetic field lines.

Magnetic reconnection between two different magnetic regions are shown in figure 2.2, e.g. the interplanetary magnetic field (red) and the Earth's magnetic field (blue). The anti-parallel magnetic field lines can reconnect as they are pushed together by an external force - in this case the constant pressure of the solar wind. Reconnected field lines, illustrated by the curved arrows in figure 2.2, have one end rooted in interplanetary space while the other is traced back into the Earth. This allows particles streaming through interplanetary space to mix with the preexisting particles in the Earth's magnetic field, ultimately altering the composition of charged particles in the ionosphere.

2.2 The Sun

The Sun is a large hot sphere of gas located in the center of our solar system, with a mass of approximately $1.99 \cdot 10^{30} kg$ and a radius of $6.957 \cdot 10^{8} m$, commonly denoted as $R_{\odot}$ (Russel et al. 2016; Stix 2012). The Sun plays an important role in the dynamics of planetary upper atmospheres and their individual ionospheres (Russel et al. 2016). It is therefore essential to obtain a basic understanding of the Sun's internal structure and atmosphere.

The Sun consists of different layers. These layers are the core, the radiative zone, the convection zone, the photosphere, the chromosphere, the transition region and the corona. The Sun's internal structure along with some observable features of its upper atmosphere, are shown in figure 2.3.

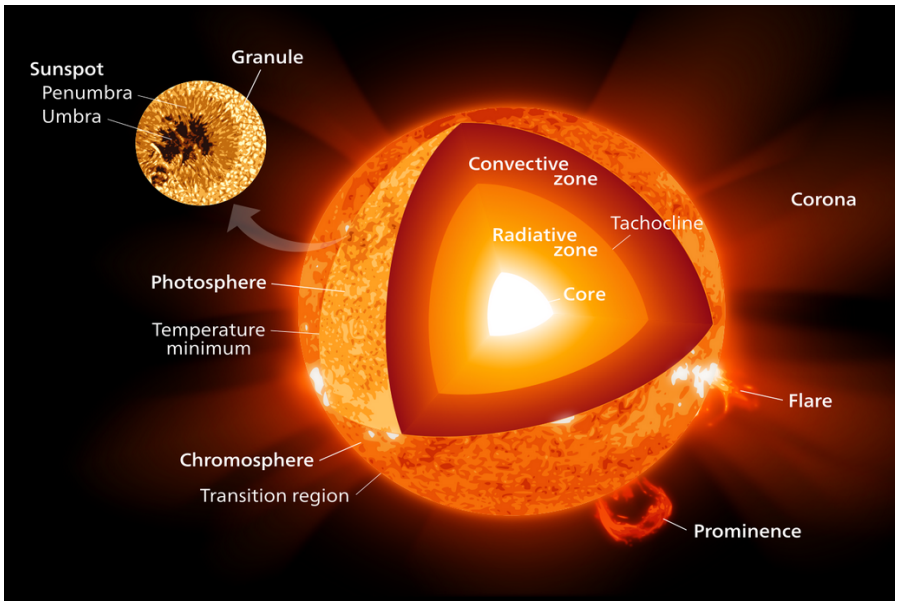

Figure 2.3: The internal structure of the Sun and some observable features originated in the Sun's upper atmosphere.
https://astrobites.org/2015/01/30/the-sun-and-its-iron-fist/

The core, located in the center of the Sun, is where the energy production takes place. The energy is produced through nuclear fusion by converting hydrogen into helium (Russel et al. 2016; Stix 2012). Nuclear fusion occurs in the innermost 20% of the Sun (Russel et al. 2016). When the energy has been produced through nuclear fusion in the core it diffuses outward into the radiative zone (Stix 2012). The released energy is in the form of electromagnetic radiation, heating the radiative zone which extends to approximately $0.7 R_{\odot}$ (Stix 2012; Russel et al. 2016).

The efficiency of radiative energy transport eventually falls, and convective energy transportation takes over (Russel et al. 2016). The energy transportation now occurs through the rise of warmer (compared to the surroundings) parcels of gas before they fall back down again after being cooled. This convective motion transfers the energy towards the Sun's surface (Russel et al. 2016; Stix 2012). As a result of the twisting and turning of the hot mixture of charged particles in the convective zone, the Sun's magnetic field is constructed.

After the convective zone, we have the photosphere. The photosphere is the *visible* part of the Sun's surface. The radiation, that has been transported through the radiative and convective zone, escapes at the photosphere. This radiation is predominantly made up of visible-light wavelengths (Russel et al. 2016), making it visible to the naked eye.

By using solar telescopes it is possible to view and study the different features prominent on the photosphere surface. Granules and sunspots are examples of interesting structures visible on the photosphere (Russel et al. 2016; Stix 2012). Granules are networks of constantly changing small-scale convection cells (Russel et al. 2016), i.e. hot parcels of gas rising due to convection. A granule is the smallest convection cell visible on the photosphere surface, and can stretch for megameters [Mm]. Supergranules can stretch for tens of megameters [Mm]. Granules are estimated to have a lifetime of tens of minutes, while supergranules can last as long as a couple of days (Russel et al. 2016). Another common feature observable on the surface of the photosphere are sunspots (Russel et al. 2016; Stix 2012). Sunspots are darker regions on the Sun's photosphere. These regions appear darker as a result of sunspots having a lower temperature than their surrounding areas. Sunspots are used to quantify the solar activity cycle, which is estimated to have a time span of 11 years (Russel et al. 2016). The dynamics of the Earth's magnetic field are heavily influenced by solar activity (McPherron 1995).

Just above the photosphere, we find the chromosphere. The chromosphere is characterized by prominences, also known as filaments (Russel et al. 2016). Prominences are large structures, in the shape of a loop, appearing on the solar disk, sometimes reaching thousands of kilometers into the Sun's corona (Russel et al. 2016; Stix 2012). Although prominences stand out as bright loops when compared to the dark background, i.e. space, they actually have a much lower temperature compared to its surroundings. It therefore can be deduced, from the lateral density equilibrium, that the density of a prominence is a lot higher than the surrounding plasma in the corona (Stix 2012). Prominences are formed over the course of minutes and typically remain stable for weeks or months (Stix 2012). The birth of prominences are known as a solar flare. Solar flares, if large enough, can alter the structure of the Earth's ionosphere (Russel et al. 2016).

The outermost regions of the Sun are the transition region and the corona, making up the upper atmosphere of the Sun. These regions have not yet been well defined (Russel et al. 2016). However, the transition region and corona are still of great interest due to the fact that the solar wind originates from these regions. As the temperature rises in the corona, it is no longer possible for the gas to maintain hydrostatic equilibrium. Meaning that the internal thermal pressure of the gas overcomes the gravitational forces of the Sun, resulting in the stream of solar wind into interplanetary space (Russel et al. 2016).

The transition region is where the chromosphere gradually develops into the corona (Russel et al. 2016; Stix 2012). The transition region fluctuates in size. This change in size is caused by local variations in the Sun's. The chromosphere-corona border mapping the transition region constantly varies, dependant on whether on not the area in question is active (Russel et al. 2016). Throughout this region the gas experiences an increase in temperature, rising from an estimated $10^4 K$ to $10^6 K$. As a result of hydrostatic equilibrium the density has to decrease rapidly in order to maintain pressure balance (Russel et al. 2016).

The corona is "the outermost solar atmosphere that most concerns space physicists because of its direct linkages to the solar wind and interplanetary magnetic field" (Russel et al. 2016, p. 116). The gas temperature in this region can reach as high as millions of degrees. With temperatures this high most of the gas is going to be ionized, making the Sun's magnetic field especially important (Stix 2012). The Sun's corona can, with its magnetic field, guide hot ionized gas through magnetic flux ropes (Dunbar 2022; Russel et al. 2016). A magnetic flux rope is formed when loops of magnetic field lines connect. It is possible for these loop-like structures to be carried away from the Sun by coronal mass ejections (CME) (Dunbar 2022). Coronal mass ejections are, along with solar flares, the most energetic coronal event (Russel et al. 2016). Resulting in high energy particles streaming through space, coronal mass ejection and solar flares can alter the Earth's ionospheric structure.

2.3 Solar Wind and Interplanetary Magnetic Field

As previously mentioned, the outermost atmospheric regions of the Sun (the transition region and corona) are of great interest as they are the source of the solar wind. The solar wind consists of particles from the sun streaming out in space while still being connected to the Sun's magnetic field (Russel et al. 2016). This is possible due to the frozen in theorem (Pécseli 2020; Russel et al. 2016). With a conductivity tending towards infinity, the magnetic field lines follow the ejected particles in the solar wind. Finding an introduction to physics of the solar wind that does not apply a form of single-fluid equations is highly uncommon (Russel et al. 2016). Magnetohydrodynamics (MHD) is a popular tool used to study solar wind dynamics due to its correlation with early measurements of the solar wind outside of the Earth's atmosphere. Additionally, the MHD fluid description correspond well with the configuration of the interplanetary magnetic field (Russel et al. 2016).

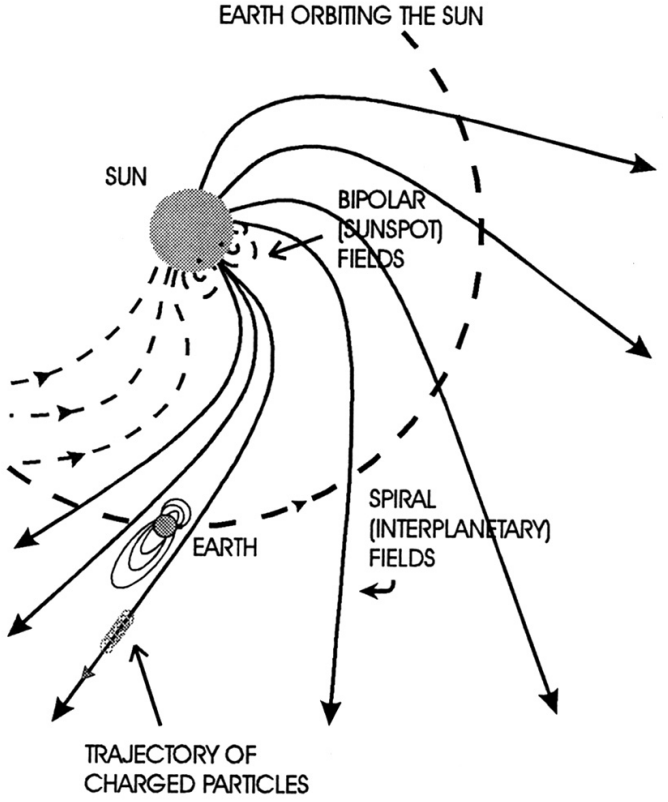

Figure 2.4: The interplanetary magnetic field leaving the Sun and passing the Earth. https://ned.ipac.caltech.edu/level5/March03/Vallee2/Vallee3_2.html

	Density	**Temperature**	**Flow Speed**
Low Speed	$8cm^{-3}$	$0.3 \cdot 10^5 K$	$300\frac{km}{s}$
High Speed	$3cm^{-3}$	$2.3 \cdot 10^5 K$	$700\frac{km}{s}$

Table 2.1: Exemplary solar wind parameters.

Typical values for density, temperature and flow speed for high and low speed solar wind can be seen in table 2.1. The solar wind flow speed remains relatively constant as the solar wind drifts towards the Earth. However, the proton and electron temperature

decrease at different rates as the solar wind flows through space. Closer to the Sun, at $0.3AU$, the proton and electron temperature is $4 - 6 \cdot 10^5 K$ and $1.5 - 2.5 \cdot 10^5 K$, respectively. Near the Earth, at $1AU$, these values decrease to $1.5 - 2.5 \cdot 10^5 K$ for the protons and $1 - 2 \cdot 10^5 K$ for the electrons (Stix 2012, p. 407). The solar wind temperature decreases as it moves earthwards from the Sun. The proton density also decreases from $0.3AU$ to $1AU$, going from $20 - 40cm^{-3}$ to $3 - 4cm^{-3}$ (Stix 2012, p. 407).

The interplanetary magnetic field generated in the Sun has the shape of a spiral as seen in figure 2.4. The spiral shape comes as a result of the Sun's continuous rotation and magnetic field lines of the Sun being frozen in the solar wind (Russel et al. 2016). As the solar wind flow speed remains largely unchanged, the spiral is approximately Archimedian (Stix 2012). However, the spiral shape of the interplanetary magnetic field is commonly known as a Parker spiral (Russel et al. 2016).

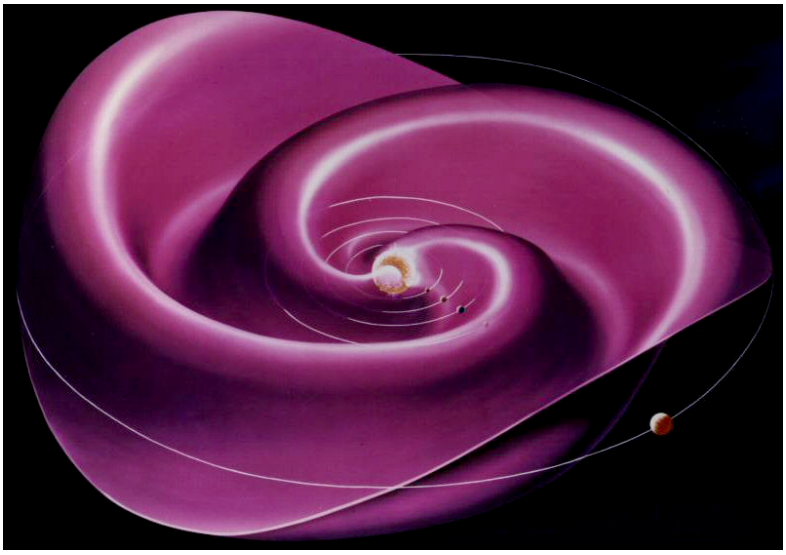

Figure 2.5: The heliospheric current sheet.
https://www.esa.int/ESA_Multimedia/Images/2019/03/Parker_spiral

The interplanetary current sheet, or heliospheric current sheet, is a thin current sheet that is created as a result of periodic changes in the polarity of the Sun's magnetic field (Russel et al. 2016). The Sun's rotational and magnetic axis are not aligned. This misalignment, in combination with the Sun's rotation, will continuously change the tilt of the current sheet resulting in the ballerina's skirt shape seen in figure 2.5. The heliospheric current sheet is considered to be the largest structure in our solar system, and extends along the equatorial plane in the heliosphere (*Parker spiral* 2022).

2.4 The Earth's Magnetosphere and Ionosphere

2.4.1 The Magnetosphere

The Earth's magnetic field is produced by the twisting and turning of the Earth's liquid core (McPherron 1995), and is offset by approximately 10.2° relative to the Earth's rotational axis (Russel et al. 2016). The magnetosphere's existence is of critical importance to life on Earth, as it acts as a shield against the solar wind and other high energetic particles (Chen 2016;Russel et al. 2016). Even though the Earth is surrounded by a magnetic field generated from currents within its core, it does not have the anticipated shape of a sphere. The Earth's magnetosphere is compressed by the interplanetary magnetic field (IMF) carried by the solar wind on its sunward side (Pécseli 2020; Russel et al. 2016). The interaction between the Earth's internally generated magnetic field and the IMF result in the shape seen in figure 2.6. The Earth's magnetosphere has a dayside and a nightside. The magnetic field lines at the magnetospheric dayside are compressed by the solar wind and closed back at the Earth's surface (Russel et al. 2016). On the contrary, the magnetospheric nightside is stretched into interplanetary space and consists of open magnetic field lines (Russel et al. 2016).

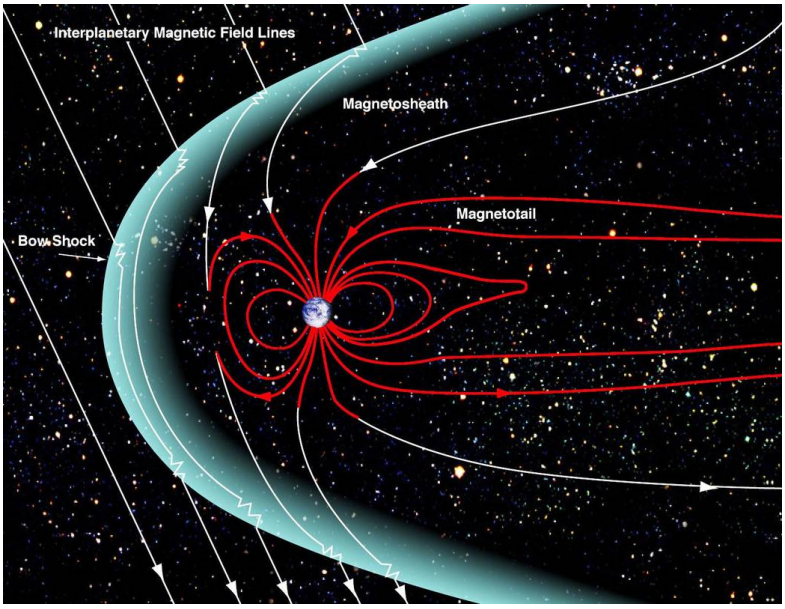

Figure 2.6: The Earth's magnetosphere with different features illustrated.
https://www.nasa.gov/mission_pages/sunearth/multimedia/magnetosphere.html

As the interplanetary magnetic field is carried by the solar wind through space it will apply pressure perpendicular to the Earth's magnetosphere, changing its size and shape due to variation in different properties of the solar wind and the interplanetary magnetic field flowing with it (Russel et al. 2016). The size and shape of the Earth's magnetosphere is determined by the balance between the Earth's magnetic pressure and the dynamic, thermal, and the interplanetary magnetic field pressure (Russel et al. 2016). Just before the solar wind reaches the Earth's magnetosphere it slows, heats and compresses at the bow shock (Russel et al. 2016). Furthermore, the speed of the solar wind decreases, from being supersonic to subsonic (Russel et al. 2016). The solar wind plasma is then deflected about the magnetosphere (Russel et al. 2016). Subsequently, the boundary

where the solar wind that has passed the bow shock collide with the Earth's magnetic field is the magnetopause. Plasma flowing in the region delimited by the bow shock and the magnetopause make up what is known as the magnetosheath (Russel et al. 2016). These features are seen in figure 2.6.

As previously mentioned, magnetic reconnection can occur when anti-parallel magnetic field lines are pushed together by external forces. Magnetic reconnection mainly takes place at two locations in the Earth's magnetic field - one being at the dayside and another on the nightside (Chen 2016; Russel et al. 2016). The magnetic reconnection on the dayside happens when the interplanetary magnetic field is anti-parallel to the Earth's magnetic field, meaning that the direction of the interplanetary magnetic field is required to be southward. Dayside magnetic reconnection is caused by the constant inflow of solar wind pushing the anti-parallel field lines together. The dayside reconnection is very sensitive to fluctuations in the direction of the interplanetary magnetic field and physical characteristics of plasma in the solar wind (Russel et al. 2016). At the nightside, reconnection occurs in the Earth's magnetotail. The magnetotail is made up of two magnetic flux tubes separated by magnetized plasma in the plasma sheet (figure 2.6). The magnetic field lines of the northern and southern lobe in the magnetotail are anti-parallel (Russel et al. 2016). Magnetic reconnection on the nightside happens as a result of the external pressure of the solar wind pushing the magnetic field lines in the magnetotail together.

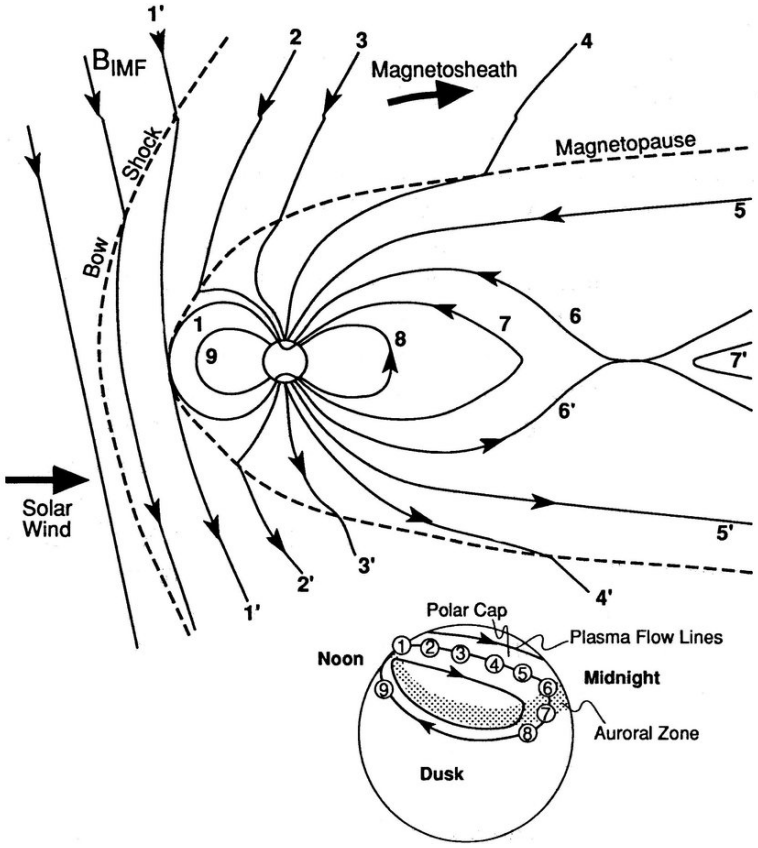

Figure 2.7: The Dungey cycle. The evolution of reconnected magnetic field lines as seen from the side and on the dusk side of the polar cap. (From Kivelson and Russell 1995).

In 1961, James Wynne Dungey, was the first in space physics research to highlight the importance of magnetic reconnection (Dungey 1961). Figure 2.7 illustrates how southward interplanetary magnetic field interact with the Earth's magnetic field, resulting in magnetic reconnection on both the dayside and the nightside. This is known as the Dungey cycle (Russel et al. 2016). The different numbers in figure 2.7 mark key aspects of the Dungey cycle. 1 and $1'$ marks the outermost closed magnetic field line of the Earth and the incoming southward interplanetary magnetic field, respectively. As these anti-parallel field lines reconnect due to pressure from the solar wind, they open up the Earth's magnetic field on the dayside. This is marked as 2 and $2'$. The constant inflow of solar wind pushes the reconnected magnetic field lines toward the nightside of the Earth, marked as 3, 4 and 5. As the external pressure from the solar wind on the magnetic field lines of the magnetotail increase they are forced together, resulting in magnetic reconnection on the nightside. The magnetotail splits into two. The left-hand side reconnects into closed magnetic field lines (6, $6'$ and 7) and the right-hand side of the magnetotail continues into interplanetary space with the solar wind ($7'$) (Chen 2016; Russel et al. 2016). Newly formed closed magnetic field lines (8) will now rotate back to the dayside of the Earth (9). This process produces two plasma convection cells - located on the dawn and dusk side of the polar cap (as seen in the bottom part of figure 2.7). The Dungey cycle can recommence if the interplanetary magnetic field remains anti-parallel to the Earth's magnetic field.

2.4.2 The Ionosphere

The Earth's upper atmosphere, the ionosphere, is of great interest in plasma and space physics given that it contains the largest accumulation of plasma in near-Earth vicinity (Pécseli 2020). Additionally, the ionosphere can be used a a tool to study the Earth's magnetospheric regions as the magnetic field lines affect the behaviour of plasma in the ionosphere.

The Earth's ionosphere is created primarily through photoionization of neutral gas due to high energy radiation from the Sun (Kelley 2009; Pécseli 2020;Russel et al. 2016). High energy wavelengths such as extreme ultraviolet and x-ray contain enough energy to partly ionize neutral molecules and atoms when absorbed in the atmosphere (Russel et al. 2016). This photoionization transforms the neutral gas into ions and free electrons, resulting in the creation of plasma (Kelley 2009; Russel et al. 2016).

The ionosphere is formed between approximately 85 and $1000km$ (Russel et al. 2016). The ionosphere is divided into different regions: the D-region (below $90km$), the E-region (between 90 and $130km$) and the F-region (above $130km$) (Russel et al. 2016). Plasma located in the E- and F-region behave differently as a result of changes in the background density of neutrals, as seen in the height density profile in figure 2.8. Changes in the plasma density is a result of the production, transportation and loss of plasma in the ionosphere (Kelley 2009; Russel et al. 2016). As previously mentioned, solar radiation is absorbed by neutrals turning them into ions and free electrons on the dayside. Thus, the density profile peaks with respect to the E- and F-region on the dayside. This is also true for the D-region. However, the regions behave differently on the nightside. In the D- and E-region the neutral density is high enough to achieve fast, dissociative recombination of molecules causing the density peak to vanish (Kelley 2009; Russel et al. 2016). Given that the F-region is made up of mostly atoms and that radiative recombination is a comparatively slow process, the F-region peak persists on the nightside (Kelley 2009; Russel et al. 2016).

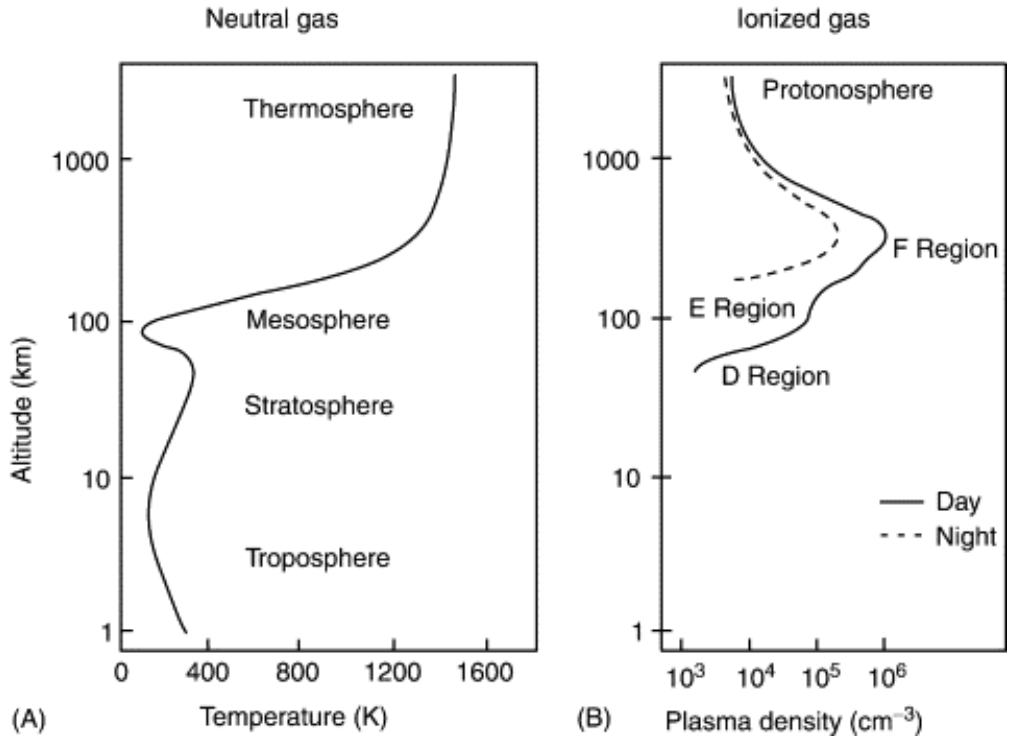

Figure 2.8: The neutral gas temperature at different altitudes of the Earth's atmosphere (A) and dayside/nightside plasma density in the ionosphere (B). (From Kelley 1989).

Magnetic field lines rooted in the Earth move through the ionosphere due to magnetic reconnection occurring on the dayside and nightside (Russel et al. 2016), as shown in figure 2.7. This result in the transportation of plasma from the dayside to the nightside and is known as ionospheric plasma convection. Given that the ionospheric plasma is formed primarily through ionizing solar radiation, it follows that the plasma density is higher on the dayside compared to the nightside. A consequence of the Dungey cycle is therefore the transportation of high density plasma located on the dayside across the polar cap towards the nightside (Lockwood and Carlson Jr. 1992). However, the ionospheric plasma convection is not a continuous process. The magnetic reconnection on the dayside, causing anti-sunward plasma convection in the polar cap, happens in bursts. These bursts tear patches of high density plasma from the dayside. As magnetic reconnection continues on the dayside the high density patches are pushed, by newly created patches, anti-sunward across the polar cap. These patches are known as *polar cap patches* (Crowley 1996) and are characterized by their plasma density being twice that of the low density plasma in the ionospheric background.

2.5 Space Weather Effects at High Latitudes

Space weather describes how variations of the Earth's immediate space environment are able to affect technological equipment (Bothmer and Daglis 2007). When limiting this to physical phenomena that are present at high latitudes, polar cap patches and plasma irregularities caused by instabilities, e.g. the gradient drift instability (GDI), are seen as significant space weather issues (Moen et al. 2013).

As technology continues to advance we become increasingly dependant on the use of different Global Navigation Satellite Systems (GNSS), not only in aviation, shipping and scientific expeditions, but in our daily lives as well. Considering that the Earth's ionosphere is made up of charged particles, i.e. plasma, signals passing through it are susceptible to scintillation. This scintillation is due to plasma irregularities and instabilities in the ionospheric structure. Scintillation and plasma instabilities are able to interfere with Very High Frequency (VHF), Ultra High Frequency (UHF) and Global Navigation Satellite Systems (GNSS) at L-band frequencies (Moen et al. 2013). Therefore, it is important to be able to understand how irregularities and structures in ionospheric plasma can negatively impact the signal quality through scintillations.

2.5.1 Gradient Drift Instability

Regions with increased plasma density (polar cap patches) have been shown to be able to negatively affect the signal quality of radio waves passing through the ionosphere (Weber et al. 1984). Multiple studies of this physical phenomenon were conducted in the years to come, both regarding polar cap patches and the gradient drift instability which is hypothesised to act on them (Gondarenko and Guzdar 2004a; Gondarenko and Guzdar 2004b; Gondarenko and Guzdar 2006; Jin et al. 2014; Weber et al. 1986).

The physical mechanism of the gradient drift instability can be seen in figure 2.9. The red line illustrates density perturbations in the trailing edge density profile of a polar cap patch. $\vec{B}$ is the Earth's magnetic field and $\vec{E_0}$ is the background electric field. The depicted polar cap patch is located in the northern polar cap and drifts anti-sunward (positive x-direction) due to the $\vec{E_0} \times \vec{B}$ drift. A charge separation occurs when a perturbation is added to the plasma density (red line), due to the fact that the positively charged ions drift rightward relative to the negatively charged electrons. This drift is known as the Pedersen drift (Tsunoda 1988; Keskinen and Ossakow 1983). This charge separation gives rise to polarization electric fields, $\vec{E_p}$. Consequently, the preexisting perturbation is further amplified as a result of the $\vec{E_p} \times \vec{B}$ drift, allowing the instability to grow. This instability (GDI) is considered to be unstable when ∇n is parallel to the bulk plasma velocity (Tsunoda 1988; Keskinen and Ossakow 1983), which happens to be the case of the trailing edge in polar cap patches.

As polar cap patches drift across the polar cap ionospheric regions, they provide suitable conditions for the gradient drift instability (GDI) (Tsunoda 1988). The gradient drift instability is an instability that acts on drifting plasma density structures. More specifically, the gradient drift instability works by breaking up the drifting density gradient of a plasma resulting in density structures ranging from meters to kilometers in scale (Gondarenko and Guzdar 2004a; Gondarenko and Guzdar 2004b; Gondarenko and Guzdar 2006; Weber et al. 1984).

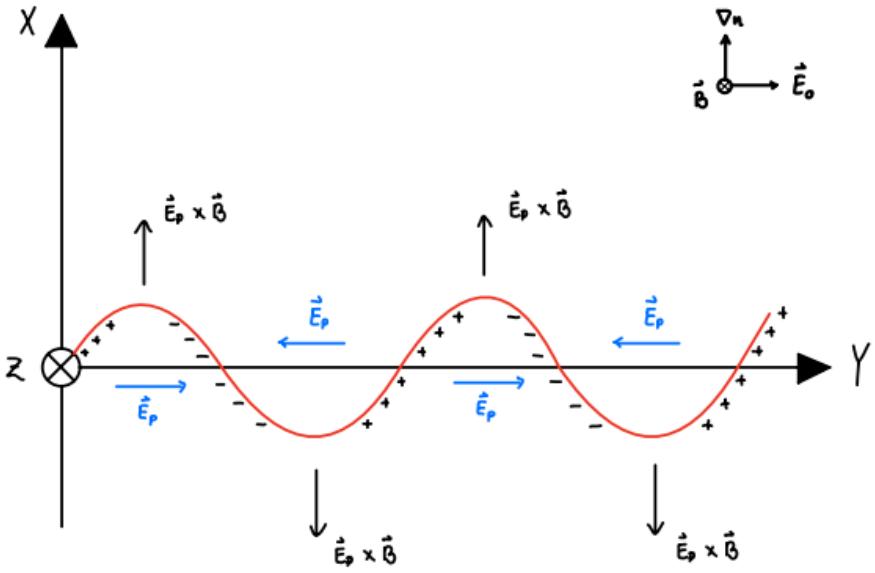

Figure 2.9: The physical mechanism of the gradient drift instability. $\vec{E_0}$ and $\vec{B}$ is the background electric and magnetic field, respectively. ∇n is the density gradient, stating that the density increases in the positive x-direction. $\vec{E_p}$ is polarization electric fields produced by charge separation.

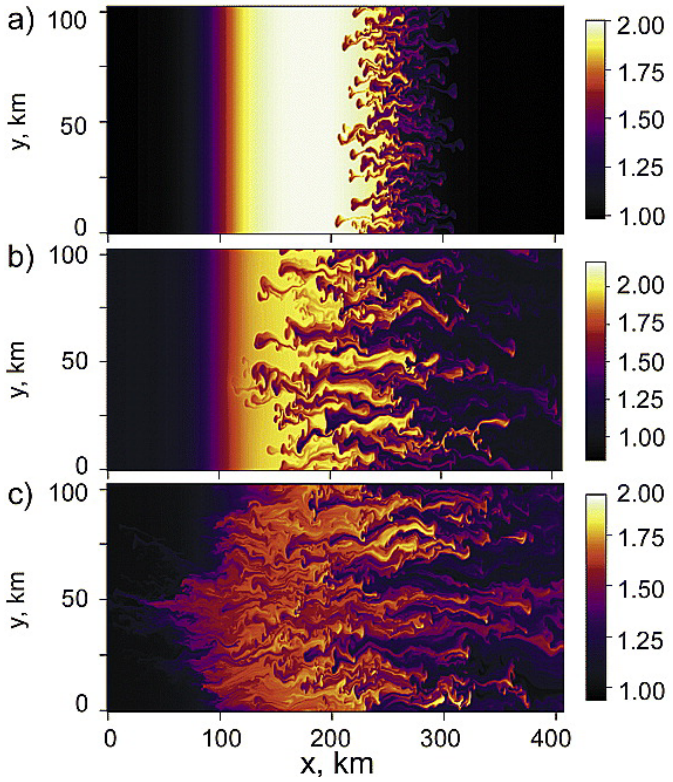

Figure 2.10: Numerical simulation of a polar cap patch drifting from right to left. The panels show the evolution of the GDI on the polar cap patch over time, starting at the topmost panel. (From Gondarenko and Guzdar 2004b).

In figure 2.10 we can see how the gradient drift instability (GDI) grows in a polar cap patch over time as it drifts from right to left. The colorbar indicates the plasma density - with bright yellow of the polar cap patch being twice that of the background density. Figure 2.10 is the result of a numerical simulation rendered in "Plasma patch structuring by the nonlinear evolution of the gradient drift instability in the high-latitude ionosphere" (Gondarenko and Guzdar 2004b). In the topmost panel the gradient drift instability has barely started to create structuring in the plasma density. Thereafter, the middle panel shows that the GDI slowly dissolves the drifting polar cap patch. As time evolves it is evident that the gradient drift instability acting on the polar cap patch form large amounts of multi-scale density structures, seen in the bottom panel.

2.5.2 Scintillation

The signals used in Global Navigation Satellite Systems are electromagnetic waves, more specifically radio waves. Electromagnetic waves do not require a medium in order to propagate through space (Chen 2016). However, they are susceptible to changes when passing through a conductive medium (e.g. a plasma). Irregularities in the conductivity of a plasma can result in disturbance of the propagating wave. This disturbance is known as scintillation.

Scintillation is defined as rapid fluctuations in phase and/or amplitude of a wave (Acharya 2015). Scintillation can occur when an electromagnetic wave is transmitted through a conductive medium with variations in its refractive index (Hutchinson 2002). Given that the transmitted GNSS signals pass through plasma in the Earth's ionosphere the received signal could exhibit changes to its amplitude and/or phase. The signal scintillation largely depends on the ionospheric conditions in its trajectory. Scintillation is divided into amplitude and phase scintillation. Amplitude scintillation negatively affects the signal quality. Phase scintillation are more common in high latitudes, i.e. the polar cap regions, and can in severe cases cause loss of lock (Petrovski and Tsujii 2012), meaning that the satellite signal is no longer tracked and has to be re-located.

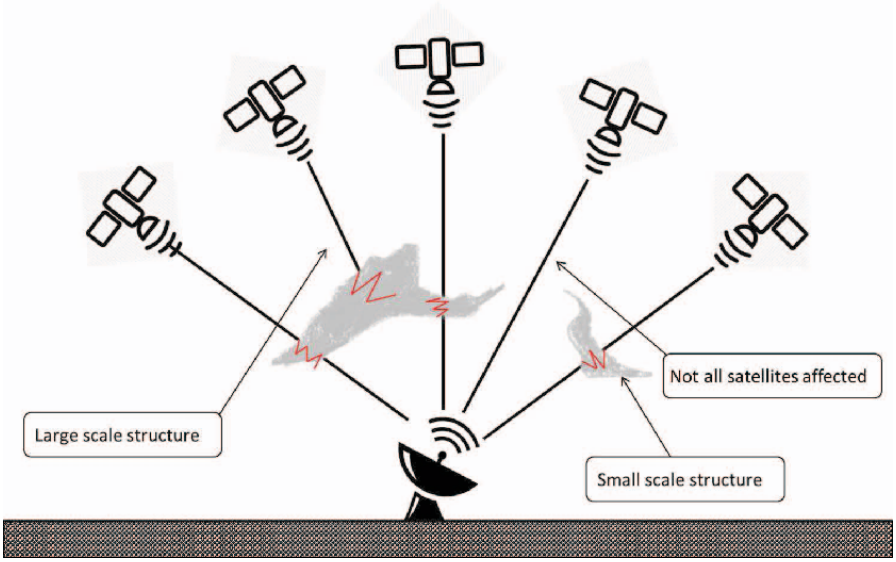

Figure 2.11: Illustration of satellite signals passing through the ionosphere. (From Aon et al. 2014).

The refractive index of a plasma is calculated using the Appleton-Hartree formula (Hutchinson 2002), and is expressed as

$$N^2 = 1 - \frac{X(1-X)}{1 - X - \frac{1}{2}Y^2\sin^2\theta \pm \left[(\frac{1}{2}Y^2\sin^2\theta)^2 + (1-X)^2Y^2\cos^2\theta\right]^{\frac{1}{2}}} \tag{2.12}$$

where $N = \frac{kc}{\omega}$ is the refractive index, $X = \frac{\omega_p^2}{\omega^2}$, $Y = \frac{\Omega}{\omega}$ and θ is the angle between the wave vector $\vec{k}$ and the magnetic field $\vec{B_0}$. Taking a closer look at the Appleton-Hartree formula (2.12), we note that the only varying parameter is the plasma frequency, $\omega_p = \sqrt{\frac{e^2 n_e}{\epsilon_0 m_e}}$. Consequently, the refractive index of a plasma only depends on the plasma (electron) density n_e. Thus, polar cap patches and the gradient drift instability (GDI) are of particular interest with respect to the use of electromagnetic signals in polar regions as they result in complex structuring of the (electron) density. This could lead to signal degrading through scintillation. This can be seen in figure 2.11. Some satellite signals are altered when passing through density variations in the ionosphere, others evade the ionospheric structures and remain relatively unaffected by scintillation.

2.6 Theory Summary

We have now seen the underlying physics in describing plasma motion using different plasma models. Utilizing the frozen in theorem we follow the plasma particles, originated in the Sun, flowing through interplanetary space with the solar wind resulting in the formation of the interplanetary magnetic field (IMF). If the IMF is anti-parallel (pointed southward) to the Earth's magnetic field, magnetic reconnection can occur and the Dungey cycle begins. This allows plasma particles from the solar wind to enter the ionosphere. Furthermore, we have discussed how the Dungey cycle transports high density plasma patches - known as polar cap patches - anti-sunward across the polar cap. Polar cap patches where then presented as a significant space weather issue due to density fluctuations caused by the gradient drift instability. These fluctuations can result in signal degrading through scintillation.

The main goal of this master thesis is to investigate the validity of previously established theories regarding the formation of complex density structures in the trailing edges of polar cap patches. More specifically, to conduct a statistical study of the occurrence of gradient drift instability in polar cap patches in polar regions. The underlying hypothesis is that the gradient drift instability acts on the trailing edges of polar cap patches. Resulting in density structures that slowly dissolve the drifting patches as seen the simulation in figure 2.10.

Additionally, this master thesis aims to conduct an interhemispheric study of the polar cap patch occurrence rate inspired by previous studies made by Chartier et al. and Spicher et al. (Chartier et al. 2018; Spicher et al. 2017). The objective of the study is to figure out whether polar cap patches have a higher occurrence rate during local winter or not - providing insight into when to expect higher amounts of signal degrading.

Chapter 3

Methodology

In this chapter the methodology of the master project will be presented. Firstly, the Swarm satellite constellation and its instrumentation used in gathering the in situ measurements of the Earth's ionosphere will be introduced. The chosen data product - IPIR - from the Swarm mission will be accounted for and explained. Furthermore, the methods of data collection, processing and analyzing will be described in detail.

3.1 Swarm Satellite Constellation: Instrumentation and Data

3.1.1 Swarm Satellites

The Swarm mission was launched on 22 November 2013 as the European Space Agency's (ESA) first constellation mission for Earth Observation (EO) (*Swarm mission* 2023). The constellation consists of three identical satellites - Alpha, Bravo and Charlie - from here on referred to as Swarm A, Swarm B and Swarm C.

The primary objectives of the Swarm mission are to study the geodynamo processes due to core dynamics, map the magnetisation of the lithosphere, and determine the electrical conductivity of the Earth's mantle in 3D. Another main objective - which is why I've chosen to work with Swarm data in my master thesis - is to investigate and understand electric currents flowing in the magnetosphere and ionosphere (*Swarm mission* 2023).

The Swarm satellites are positioned in low Earth orbits (LEO) across the polar regions of the northern and southern hemisphere and use identical instruments in order to study the dynamics of the Earth's space environment. The plasma density - used in identifying polar cap patches and central for this master thesis - is measured using two Langmuir probes mounted underneath the satellite (*Swarm mission* 2023) as seen in figure 3.1. The Thermal Ion Imagers are able to detect the plasma ion distribution - providing information regarding the ion drift velocity (*Swarm mission* 2023).

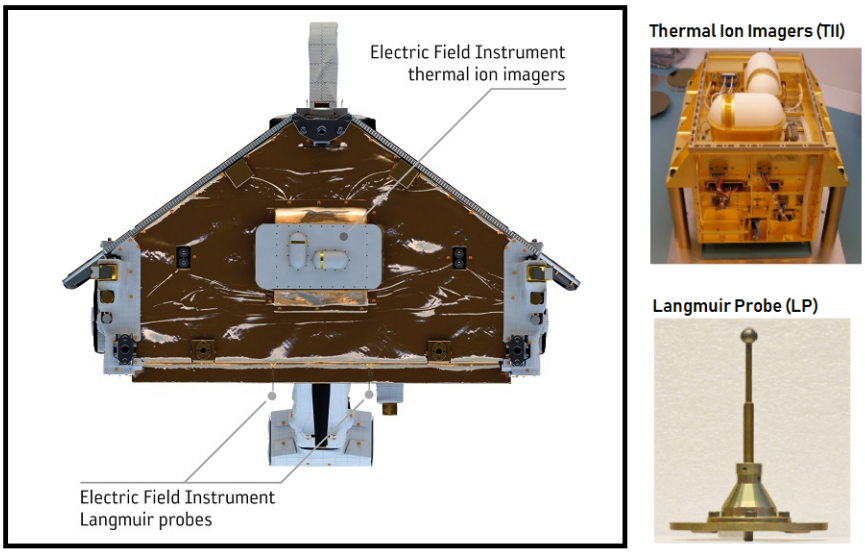

Figure 3.1: Swarm satellite viewed from the front. Instruments used to measure electric field - Thermal Ion Imagers and Langmuir Probes - are shown in greater detail. (From *Swarm mission* 2023).

3.1.2 The Chosen Data Product - IPIR

A suitable data project had to be selected before the work towards testing the master project's hypothesis could begin. The data product had to be applicable with respect to a polar cap patch study. This meant that the data product had to contain when and where the satellites were located at a given time (positional data), and plasma density measurements. Furthermore, polar cap patch flag data would be a desirable parameter as this has been beneficial in previous studies such as Spicher et al.'s interhemispheric polar cap patch study (Spicher et al. 2017). The polar cap patch flag indicates whether the satellite measurements were taken within a polar cap patch. Additionally, the polar cap patch flag is used to identify polar cap patch edges. The physical implication of the polar cap patch flag (PCP_flag) can be seen in table 3.1.

PCP_flag value	**Physical implication**
0	Outside PCP
1	PCP edge
2	PCP leading edge
3	PCP trailing edge
4	PCP proper

Table 3.1: Physical implication of the polar cap patch flag values in the IPIR data product (Jin et al. 2022).

Therefore, the choice fell on the newly developed Ionospheric Plasma IRregularities (IPIR) data product (Jin et al. 2022), which the European Space Agency has made available for download at *Swarm Data Access* 2023. The IPIR data product was developed to facilitate extensive studies of ionospheric plasma structuring and variability in the ionosphere over the span of multiple years (Jin et al. 2022). Additionally, IPIR was created to provide a reference dataset in order to prevent discrepancy between studies of similar problems due to differences in processing algorithms (Jin et al. 2022).

3.1.3 How the Data Was Used

The primary tool that has been utilized when working with this master project is Python. Given that the data product, IPIR, is formatted using the Common Data Format (CDF) it would be beneficial to use the Python package SpacePy (Morley et al. 2011) in order to read and systematize the downloaded satellite data. SpacePy is designed for space science usage, and provides a fast, easy to use data collection method (Morley et al. 2011). Once the CDF-files containing the satellite data, from mid 2014 to the end of 2019, had been downloaded the SpacePy package could be implemented to store arrays containing parameters of interest. The chosen parameters were longitude, latitude, radius (satellite orbital height), timestamp, N_e (electron density) and the PCP_flag. Measurements taken between latitudes of 77 degrees and -77 degrees were removed using a short snippet of code. This was done due to the fact that the regions of interest in the polar cap patch studies in this master thesis are the polar regions.

However, since the IPIR data product does not contain magnetic latitude (MLAT) data or magnetic local time (MLT) data this had to be generated. The MLAT and MLT data is used to identify polar cap patch edges later on. MLAT and MLT data was generated using ApexPy in Python (Meeren et al. 2023). ApexPy is a Python wrapper that allows converting between geodetic coordinates, and magnetic latitude (MLAT) and magnetic local time (MLT) using the International Geomagnetic Reference Field (Meeren et al. 2023; Emmert et al. 2010; Alken et al. 2021). The conversion takes latitude, longitude, measurement altitude and time as parameters.

Now that the Swarm data from the IPIR data product had been stored locally and the magnetic latitude (MLAT) and magnetic local time (MLT) data had been generated the work on the polar cap patch gradient drift and climatology study could commence.

The Study of Gradient Drift Instability in Polar Cap Patches

The IPIR data product was chosen much due to the PCP_flag parameter. The PCP_flag uses ion drift velocity - measured using the Thermal Ion Imagers - to distinguish the trailing and leading edge of polar cap patches. However, the Thermal Ion Imagers have not been functioning properly, resulting in no PCP_flag values indicating the leading or trailing edge. The only PCP_flag values were therefore 0, 1 and 4.

An algorithm used to locate trailing and leading edges of the polar cap patches had to be created in order to further investigate fluctuations in density that could come as a result of the gradient drift instability. This was achieved using the PCP_flag data. As previously mentioned, the PCP_flag data provides indices to each identified polar cap patch proper and edges. However, the downloaded data product, IPIR, did not say whether the edge was the trailing or the leading edge. The trailing and leading edge had to be identified through an alternate method.

Firstly, the indices of where the individual polar cap patch started and ended were determined using Python. This was simply done by comparing the original PCP_flag data array with two shifted copies to locate where the index changes from $0 \rightarrow 1$ and vice versa - one copy shifted one element to the right and the other shifted leftwise. The exact same algorithm was applied to locate the polar cap patch proper's start and end, where the index changes from $1 \Leftrightarrow 4$.

Knowing where the polar cap patch edges were found in the measurements, they had to be defined as either a trailing or a leading edge. This was achieved by using a combination of the ApexPy generated MLAT and MLT data in addition to the indices regarding the beginning and end of the polar cap patch edges and proper. Firstly, the dayside and nightside of the Earth were split into different sectors using magnetic local time (MLT), as shown in figure 3.2. Each individual start and end of a given polar cap patch were then compared with each other with respect to their magnetic latitude. For polar cap patches located on the dayside the leading edge is from this point forward defined as the one located at the highest absolute value of the magnetic latitude with the trailing edge following behind at a lower magnetic latitude. The argument is flipped on the nightside; the edge located at the lowest magnetic latitude is the leading edge. Trailing and leading edges of the polar cap patch where then paired with the start and end of the polar cap patch proper indices. Subsequently, the index of the beginning and end of each trailing and leading edge were established.

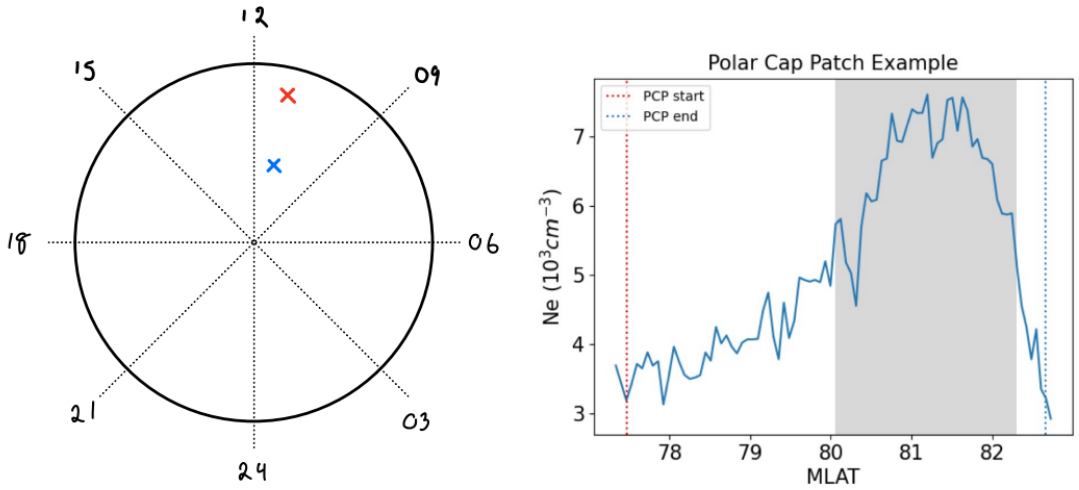

Figure 3.2: The figure on the left hand side illustrates the different magnetic local time sectors. The right hand side is a density plot of an actual polar cap patch located and used in this master project. The polar cap patch start and end are shown using red and blue dotted lines, respectively. Additionally, the PCP beginning and end is illustrated in its MLT sector using a red and a blue *X*. The polar cap patch proper is delimited by the grey background.

Figure 3.2 shows how the magnetic local time sectors were divided. Additionally, the figure provides an example of an actual polar cap patch and how the trailing and leading edge were determined. The polar cap patch was found in the MLT $9 - 12$ sector. Subsequently, the magnetic latitude of its start (red dotted line) and end (blue dotted line) were compared. The region between the PCP start and PCP proper was determined as the trailing edge, given that the polar cap patches drift anti-sunward across the polar cap. The leading edge was assigned to be the region on the right hand side of the PCP proper.

The polar cap patch measurements were then divided into different sectors based on magnetic local time. This was done to better compare patches located at different stages in their convection across the polar cap. Additionally, a series of conditions were applied: both edges of the polar cap patch had to be located in the same MLT sector, the polar cap patch is required to span over at least 1 degree of magnetic latitude, at least

one of the data points had to be inside a polar cap patch proper (PCP_flag = 4) and the polar cap patch had to meet a length requirement of 15 data points (corresponding to approximately $100km$).

In order to analyze and study whether or not the gradient drift instability (GDI) affected the trailing edge of a polar cap patch to a greater extent than the leading edge, a linear regression model was implemented. The linear regression model in question is from the Scipy Python package, and is called stats.linregress. Stats.linregress calculates the best fitted line (linear regression) of a dataset (Virtanen et al. 2020). Additionally, it returns the standard deviation (σ) of the linear regression (Virtanen et al. 2020) which is central to my gradient drift instability polar cap patch study.

The reasoning behind the use of the standard deviation to investigate GDI in polar cap patches is that I believe that the gradient drift instability results in greater fluctuations in the trailing edge when compared to the leading edge. This would indicate that the trailing edge density measurements deviate more from the regression line in comparison to that of the leading edge. Because of this the linear regression which also provides the standard deviation were calculated for each individual patch, both in the leading and trailing edge, before they were used to calculate a standard deviation ratio:

$$f = \frac{\sigma_{\text{te}}}{\sigma_{\text{le}}} \tag{3.1}$$

where f is the standard deviation ratio, and σ_{te} and σ_{le} is the standard deviation in the trailing and leading edge, respectively. The ratio, f, were then used in order to create statistical plots such as boxplots and histograms to study the occurrence of gradient drift instability in polar cap patches. The physical meaning of the standard deviation ratio, f, were established as seen in table 3.2.

Standard deviation ratio f	**Physical implication**
$f < 1$	No Gradient Drift Instability
$1 \leq f < 2$	Inconclusive
$f \geq 2$	Gradient Drift Instability

Table 3.2: Physical implication of the standard deviation ratio f.

The Polar Cap Patch Climatology Study

After the polar cap patch gradient drift instability study I wanted to conduct an interhemispheric study on the occurrence of polar cap patches in order to quantify when to expect greater impact on GNSS signal quality - still using the newly developed IPIR data product (Jin et al. 2022). This study is inspired by previous studies done by Spicher et al. and Chartier et al. (Spicher et al. 2017; Chartier et al. 2018).

This polar cap patch climatology study was developed using the same data as the polar cap patch gradient drift instability study. More specifically, it uses the median index of the start and end of each individual polar cap patch to identify when it occurred. The polar cap patch indices were then used in a method to count the patch occurrence. A method aimed at finding the time each satellite spent over the northern and southern polar cap was also created, i.e. hours above 77 degrees MLAT for the northern hemisphere and hours below -77 degrees MLAT for the southern hemisphere. The resulting number of occurrences were then divided by the hours spent above the polar caps for each individual date and plots were made for the northern and southern

hemisphere. Summer and winter time were defined with respect to the local season in the northern hemisphere and visualized on both plots. The winter time period was defined to be between the autumnal equinox (September 24) and the vernal equinox (March 20).

Now that the theoretical foundation has been laid and the methodology of both the polar cap patch gradient drift instability and climatology study have been explained, the collected Swarm data can be processed and further studied with respect to the underlying hypothesis of this master thesis.

Chapter 4

Observations and Results

The purpose of the following chapter is to present the results that have been gathered through the processing of the IPIR data product containing data from the Swarm mission. The chapter is divided into two different sections, beginning with the resulting plots regarding the polar cap patch gradient drift instability study. Thereafter, results from the polar cap patch climatology study - providing better insight into when polar cap patches are prone to affect signal quality - are presented.

A grand total of 8092 polar cap patches were located and processed using the methodology described in the previous chapter (3). Both studies take advantage of the total amount of polar cap patches. The polar cap patch gradient drift study's results are expressed using multiple statistical plots. These plots are histograms and bar charts of the standard deviation ratio, f, explained in detail in the methodology chapter (3). The resulting plot in the polar cap patch climatology study is a scatter plot of the polar cap patch occurrence rate in the northern and southern hemisphere.

The standard deviation ratio, f, indicates differences between the trailing and leading edge in polar cap patches (chapter 3). Low f-ratio values ($0 < f < 2$) suggest little to no difference in plasma density structuring are found in the thin, leftmost bin. Meanwhile, bigger f-ratios ($2 \leq f$) indicate greater differences between the tailing and leading edge and the likeliness of GDI impact, occupying the remaining bins. It is therefore important to be aware of this asymmetry when viewing the histograms presented in this chapter.

4.1 Polar Cap Patch Gradient Drift Instability Study

4.1.1 MLT Noon and Midnight Sectors

Figure 4.1 shows how the standard deviation ratio, f, varies in occurrence number in different magnetic local time sectors in the northern hemisphere. The top row consists of magnetic local time sectors situated on the Earth's dayside, while the bottom row are located on the nightside. A common trait in the four MLT plots in figure 4.1 is that the majority of the standard deviation ratios have values less than 30.

The plots do however differ when considering values above $f = 30$. For MLT $9 - 12$, the f-ratio occurrence number decreases rapidly above $f = 30$ before experiencing a slight increase for values between $40 - 60$. The occurrence number in the MLT $12 - 15$ and $0 - 03$ sectors both decrease gradually with increasing f-ratios. Fluctuations in the occurrence number are noticeable with increasing standard deviation ratios in the lower left plot (MLT $21 - 24$). MLT $12 - 15$ and $21 - 24$ have a hand full of ratios above $f = 60$.

The data visualized in figure 4.2 is calculated using standard deviation ratios in polar cap patches detected in the southern hemisphere, and shows similar traits as figure 4.1. The majority of f-ratios are located below $f = 30$. A noteworthy distinction is that there is a higher occurrence number of larger standard deviation ratios in the bottom plots, MLT $21 - 24$ and $0 - 03$.

4.1.2 MLT Dawn and Dusk Sectors

MLT sectors situated at the dawnside and duskside of the Earth are shown in figure 4.3 and figure 4.4. The dawnside is made up by the MLT $6 - 9$ and $3 - 6$ sectors, while the duskside consists of MLT $15 - 18$ and $18 - 21$. Dayside magnetic local time sectors are found in the top row with nightside residing in the bottom row.

Figure 4.3 consists of standard deviation ratios calculated using polar cap patches in the northern hemisphere. The plots in the bottom row and top right viewed in figure 4.3 show quite similar trends regarding the occurrence number of the standard deviation ratio f. The majority of f-ratios are found below approximately $f = 30 - 40$. However, when comparing the top and bottom row there appears to be a higher occurrence number of larger f-ratios in the MLT $18 - 21$ and $3 - 6$ plots. The MLT $6 - 9$ plot in figure 4.3 shows only three f-ratios above $f = 50$.

Dawnside and duskside MLT sectors in the southern hemisphere can be seen in figure 4.4. Once again, there is a noteworthy higher occurrence number of standard deviation ratios below $f = 40$ in comparison to larger values. The magnetic local time sectors in the bottom row contain multiple large f-ratios above $f = 30 - 40$. In contrast, there are almost no standard deviation ratios above $f = 40$ in the upper row in figure 4.4.

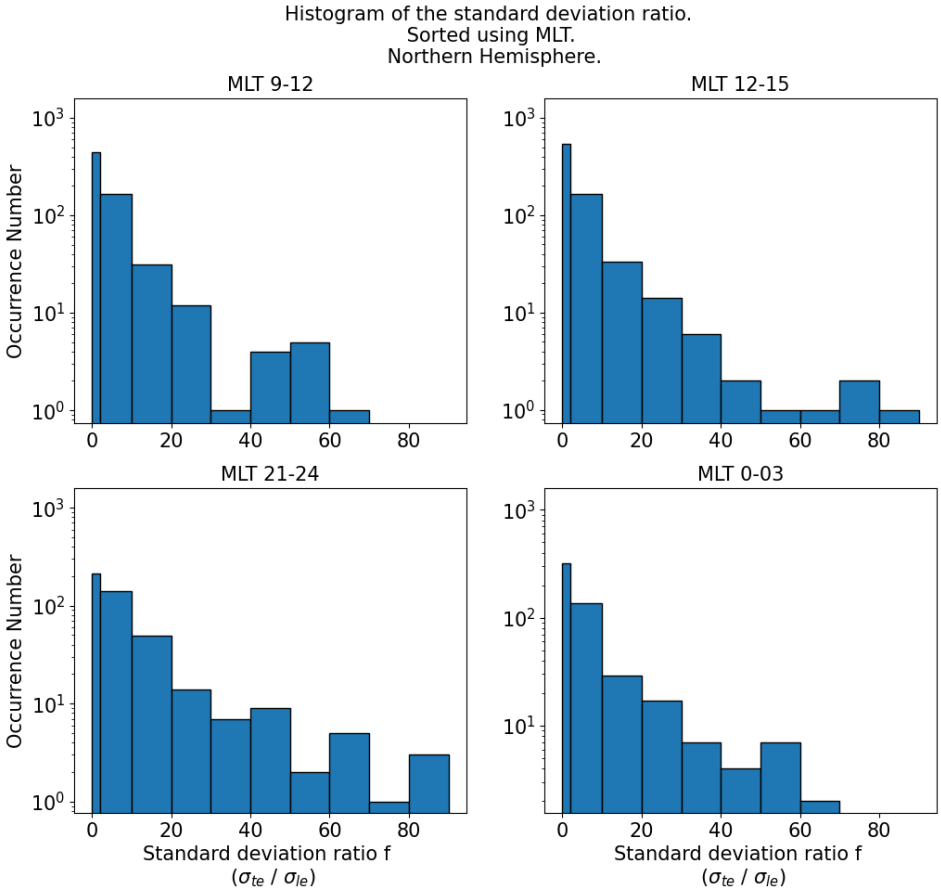

Figure 4.1: Histogram that shows the standard deviation ratio's occurrence number in the northern hemisphere. The y-axis shows how often the ratios occur and the x-axis is divided into bins. The first two bins contain $f \in [0, 2\rangle$ and $f \in [2, 10\rangle$, respectively. Subsequently, the bins increment by a value of ten. The ratios are categorized into different magnetic local time (MLT) sectors; $9-12$ (top left), $12-15$ (top right), $21-24$ (lower left) and $0-03$ (lower right).

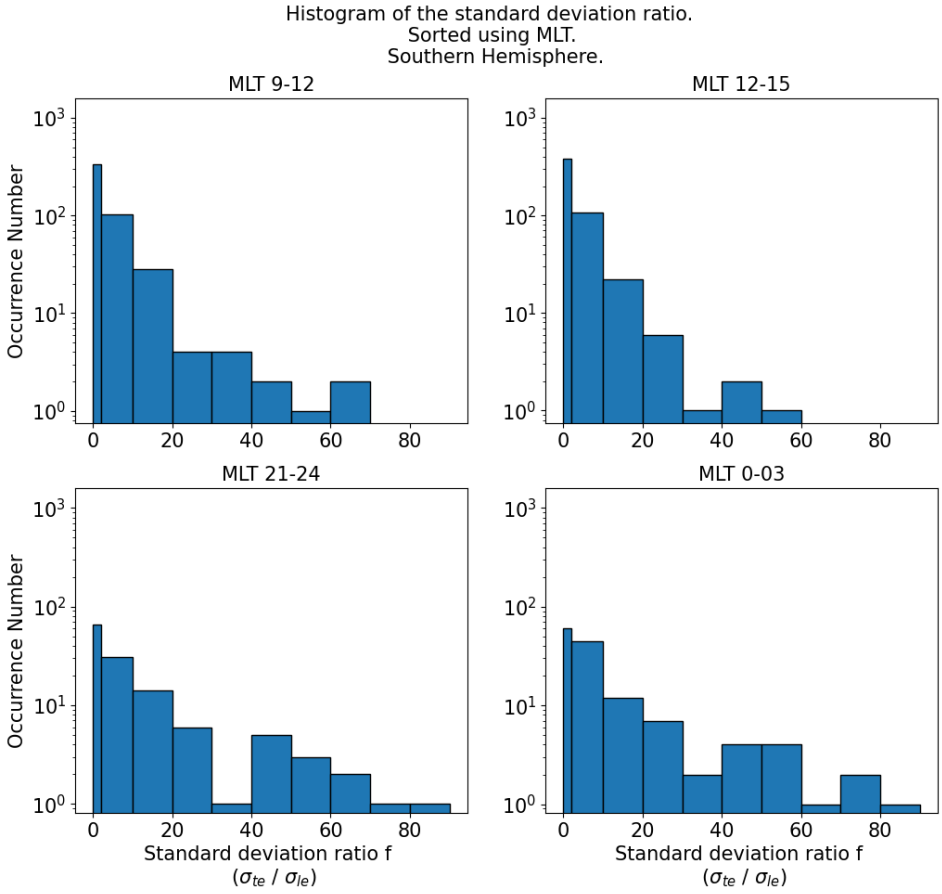

Figure 4.2: Histogram that shows the standard deviation ratio's occurrence number in the southern hemisphere. The y-axis shows how often the ratios occur and the x-axis is divided into bins. The first two bins contain $f \in [0, 2\rangle$ and $f \in [2, 10\rangle$, respectively. Subsequently, the bins increment by a value of ten. The ratios are categorized into different magnetic local time (MLT) sectors; $9-12$ (top left), $12-15$ (top right), $21-24$ (lower left) and $0-03$ (lower right).

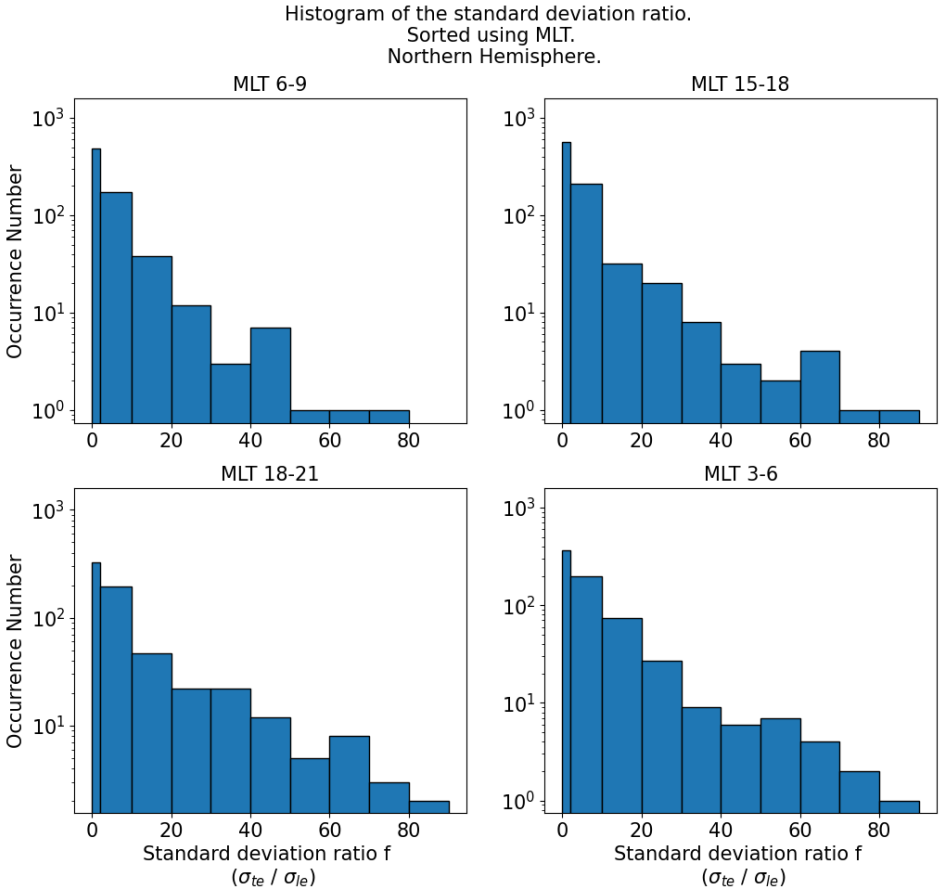

Figure 4.3: Histogram that shows the standard deviation ratio's occurrence number in the northern hemisphere. The y-axis shows how often the ratios occur and the x-axis is divided into bins. The first two bins contain $f \in [0, 2\rangle$ and $f \in [2, 10\rangle$, respectively. Subsequently, the bins increment by a value of ten. The ratios are categorized into different magnetic local time (MLT) sectors; $6-9$ (top left), $15-18$ (top right), $18-21$ (lower left) and $3-6$ (lower right).

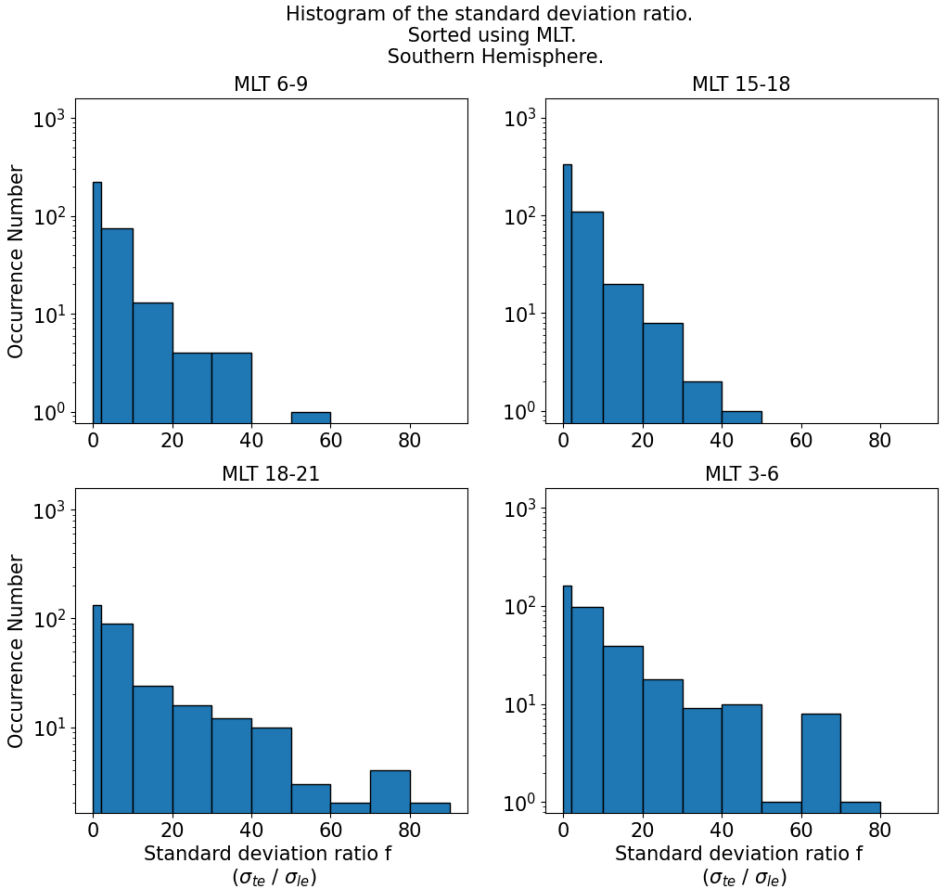

Figure 4.4: Histogram that shows the standard deviation ratio's occurrence number in the southern hemisphere. The y-axis shows how often the ratios occur and the x-axis is divided into bins. The first two bins contain $f \in [0, 2\rangle$ and $f \in [2, 10\rangle$, respectively. Subsequently, the bins increment by a value of ten. The ratios are categorized into different magnetic local time (MLT) sectors; $6 - 9$ (top left), $15 - 18$ (top right), $18 - 21$ (lower left) and $3 - 6$ (lower right).

4.1.3 Dayside and Nightside Comparison

The following plots (4.5 & 4.6) were made to better emphasize differences in the standard deviation ratio occurrence number between polar cap patches situated on the dayside and nightside of the Earth.

Minimal changes in the f-ratio occurrence number are noticeable when comparing the standard deviation ratios below $f = 30$ in the dayside and nightside viewed in figure 4.5a and 4.5b. This also applies to 4.6a and 4.6b. However, an increase in f-ratio occurrence number is visible when concerning larger standard deviation ratios.

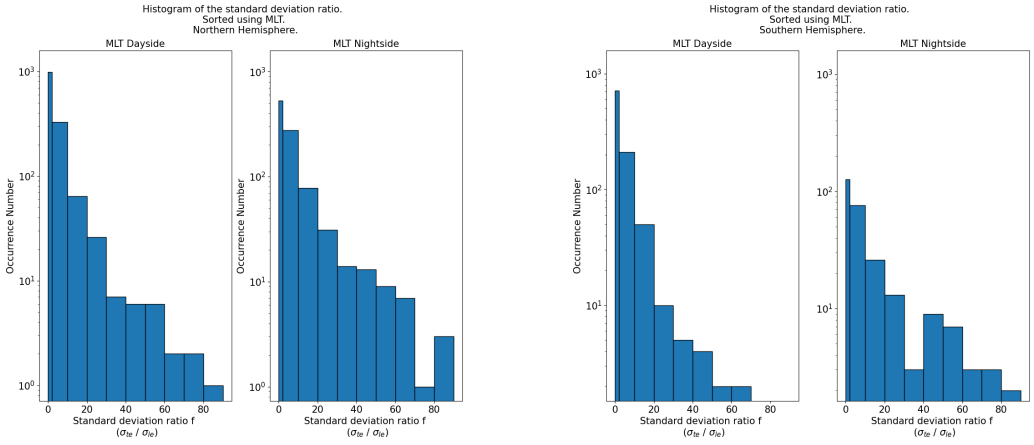

(a) (b)

Figure 4.5: Histograms comparing the dayside and nightside occurrence number of the standard deviation ratio f in the noon/midnight MLT sectors. Both the northern hemisphere (4.5a) and southern hemisphere (4.5b) are shown.

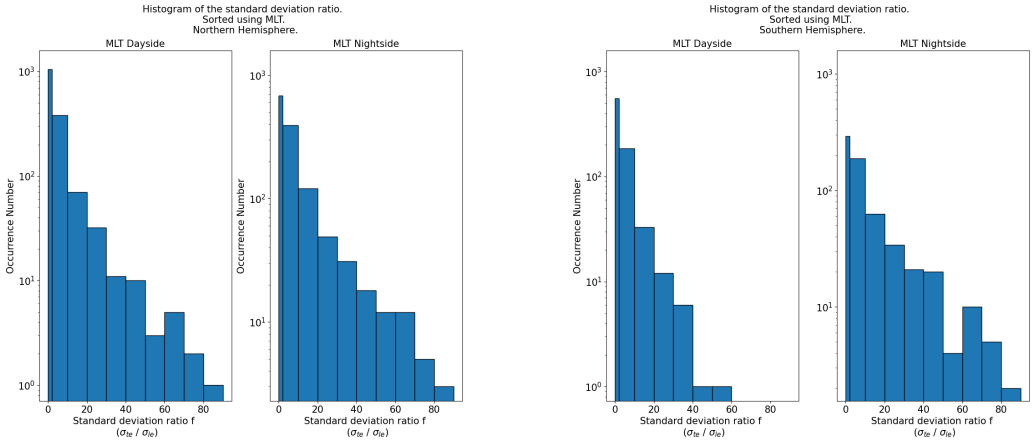

(a) (b)

Figure 4.6: Histograms comparing the dayside and nightside occurrence number of the standard deviation ratio f in the dawn/dusk MLT sectors. Both the northern hemisphere (4.6a) and southern hemisphere (4.6b) are shown.

4.1.4 Physical Implications

Figure 4.7 and 4.8 illustrate the physical implication of the standard deviation ratio, f, as described in the methodology chapter (3). The f-ratio value provides information on whether the polar cap patches have been affected by the gradient drift instability.

Figure 4.7 shows magnetic local time sectors surrounding noon and midnight. MLT $9-12$ and $12-15$ (located on the dayside) show similar characteristics in both the northern and southern hemisphere. f-ratios below 1 occur in almost twice the amount of patches when compared to $f \geq 2$. In nightside sectors (MLT $21-24$ and $0-03$) however, the number of polar cap patches where the standard deviation ratio between the trailing and leading edge is greater than or equal to 2 ($f \geq 2$) is larger than that of $f < 1$. This is visualized with the green bars being taller than the red bars. $1 \leq f < 2$ (blue bars) remain approximately unchanged from the dayside to the nightside in the northern hemisphere, while they decrease in the southern hemisphere.

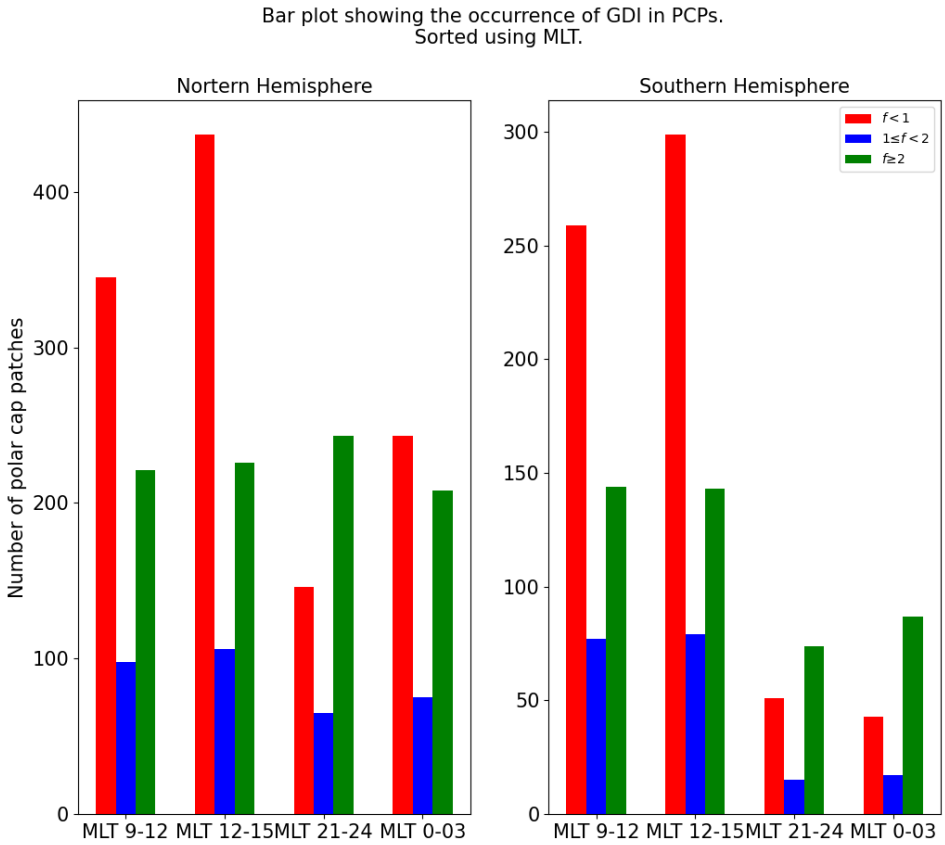

Figure 4.7: Bar charts showing the physical implication of the standard deviation ratio, f. The colors represent different f-ratio values. Red represents polar cap patches where $f < 1$ and blue where $1 \leq f < 2$. Green represents $f \geq 2$. The x-axis shows different magnetic local time sectors and the y-axis shows the number of polar cap patches.

The magnetic local time sectors encompassing dawn and dusk and their respective polar cap patch f-ratios can be seen in figure 4.8. The blue bars ($1 \leq f < 2$) stay somewhat constant in both hemispheres. Focusing on MLT $6-9$ and $15-18$ we notice that there are more polar cap patches with low f-ratio values ($f < 1$) compared to other values. Polar cap patches with high f-ratio values dominate in the nightside magnetic local time sectors (MLT $18-21$ and $3-6$) in both hemispheres.

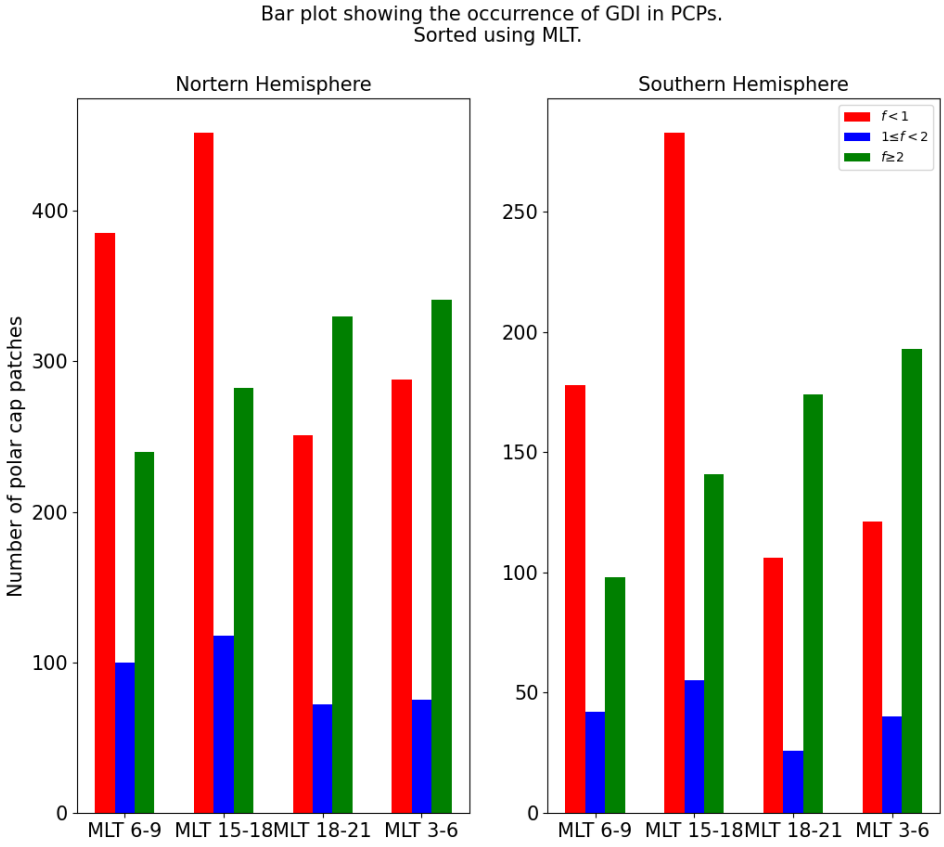

Figure 4.8: Bar charts that show the physical implication of the standard deviation ratio, f. The colors represent different f-ratio values. Red represents polar cap patches where $f < 1$ and blue where $1 \leq f < 2$. Green represents $f \geq 2$. The x-axis shows different magnetic local time sectors and the y-axis shows the number of polar cap patches.

4.2 Polar Cap Patch Climatology Study

Lastly, we have the polar cap patch climatology study investigating polar cap patch formation trends. This study aims to determine when we can expect higher impact on GNSS signal quality due to the presence of polar cap patches. Figure 4.9 shows the occurrence rate of polar cap patches in the northern hemisphere (upper panel) and southern hemisphere (bottom panel) spanning over multiple years. Each data point symbolizes the amount of polar cap patches on a given date, divided by the hours spent above $|MLAT| = 77°$ (denoted as $\#/h_{PC}$) by the Swarm satellite. Yellow background indicates local summer conditions while blue background indicates local winter.

In the top panel in figure 4.9 we can clearly observe that the occurrence rate of polar cap patches is higher during local winter conditions in the northern hemisphere. The polar cap patch occurrence rate achieves values as high as $2.5\#/h_{PC}$ during local winter conditions. In comparison, the occurrence rate rarely reaches as high as $0.5\#/h_{PC}$ during local summer.

The occurrence rate of polar cap patches in the southern hemisphere is shown in the bottom panel of figure 4.9. The polar cap patch occurrence rate appears to display similar trends in the southern hemisphere when compared to the northern hemisphere. The occurrence rate reaches values between $1.5-2\#/h_{PC}$ during local winter conditions. During local summer the occurrence rate only reaches a maximum of $1\#/h_{PC}$.

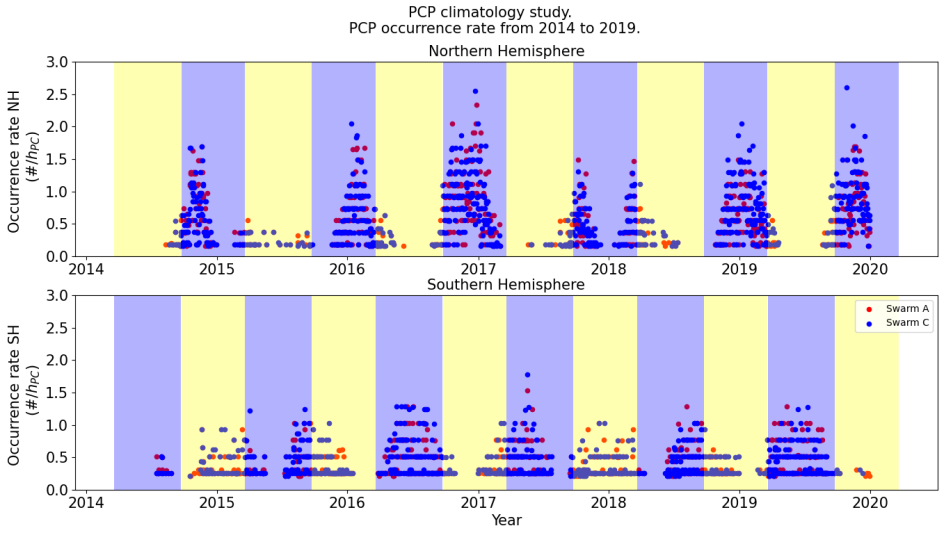

Figure 4.9: Scatter plot showing the occurrence rate of polar cap patches in the northern (top panel) and southern hemisphere (bottom panel). Red data points are measurements taken by Swarm A. Blue data points are measurements from Swarm C. The blue and yellow background color indicate local winter and local summer conditions, respectively.

Chapter 5

Discussion

Now that the observations and results from both the polar cap patch gradient drift instability study and the polar cap patch climatology study have been presented, we will discuss the differences and physical implications of the aforementioned results. The following chapter is split in two. We begin with discussing the results of the gradient drift instability study before taking a closer look at the climatology study.

5.1 Polar Cap Patch Gradient Drift Instability Study

The underlying hypothesis of the polar cap patch gradient drift instability study is that the gradient drift instability acts on the trailing edge of polar cap patches. This should, in theory, result in the polar cap patch dissolving from behind. In order to be able to provide evidence to support this master project's hypothesis we introduced a set of physical implications with respect to the f-ratio. The physical implications were presented in chapter 3 and are shown in table 3.2. The direct comparison of the trailing and leading edge standard deviation was chosen despite the fact that ionospheric plasma is likely to be affected by different types of instabilities and turbulence when drifting across the polar cap regions. The reasoning behind this choice is that I believe that other instabilities and turbulence affect the trailing and leading edge to similar degree, resulting in the gradient drift instability being the primary source of variation in plasma density structuring.

Let us begin with examining the histograms in figure 4.1 and 4.2. They both present the calculated standard deviation ratio, f, in the magnetic local time sectors surrounding noon and midnight. Figure 4.1 and 4.2 also illustrate calculations in the northern and southern hemisphere, respectively. We quickly notice that standard deviation ratios where $0 < f < 2$ occur more frequently compared with larger f-ratio values. It is therefore possible to argue that there is a high number of polar cap patches used in this study that show little to no difference when considering plasma density structuring in the leading and trailing edge. In other words; there is a large number of polar cap patches where whether the gradient drift instability affects the trailing edge to a greater extent is inconclusive or even incorrect.

However, further inspection of figure 4.1 and 4.2 show varying amounts of greater f-ratio values. High standard deviation ratios could indicate greater differences in the trailing and leading edge density profiles of the polar cap patches. With respect to the underlying hypothesis this implies that the gradient drift instability appears to be present in all magnetic local time sectors, although not affecting every polar cap patch to the same degree.

Figure 4.3 and 4.4, showing f-ratios in the dusk/dawn sectors, exhibit similar traits as the aforementioned noon/midnight sectors (4.1 & 4.2). Once again, we notice that lower standard deviation ratios are most frequent. When comparing the dayside and nightside magnetic local time sectors, we notice a small decrease in inconclusive standard deviation ratios ($0 < f < 2$). Additionally, a significant increase of higher f-ratios is apparent.

These findings become more evident when comparing the total dayside and nightside standard deviation ratio occurrence number, as seen in figure 4.5 and 4.6. We observe a total decrease in low standard deviation ratios, f, and an increase in higher f-ratios from the dayside to nightside. This can be seen in correlation with the anti-sunward drift of polar cap patches in the polar regions. High density plasma patches are transported across the polar cap regions through the Dungey cycle as a result of dayside magnetic reconnection. Consequently, the polar cap patches start their journey across the polar cap in the magnetic local time sectors situated on the dayside. Given that the gradient drift instability is an instability that develops on *drifting* plasma density structures, it is reasonable to assume that the GDI impact would be relatively small on the dayside when compared to polar cap patches on the nightside due to the comparably short drift-time. Thus, strengthening the scientific hypothesis stating that the gradient drift instability results in the formation of complex density structures in the trailing edge of polar cap patches.

Lastly, we take a more direct approach to investigate the physical implications of the standard deviation ratio calculations. Figure 4.7 and 4.8 are bar charts that show the physical implications (explained in chapter 3 and table 3.2) of the polar cap patch f-ratios. Red indicates polar cap patches with no gradient drift instability, blue is inconclusive results and green symbolizes the occurrence of gradient drift instability.

Looking at the first bar chart (figure 4.7) we see that the majority of polar cap patches found in the dayside magnetic local time sectors (MLT $9-12$ and $12-15$) have low f-ratio values. This could mean that they are not yet affected by the gradient drift instability. However, a significant amount of GDI affected polar cap patches are located as well. When locating the polar cap patches using the PCP_flag data we only categorize them into different magnetic local time sectors, not accounting for their location in the given sector. This could result in polar cap patches being located at a multitude of magnetic latitudes. Meaning that two polar cap patches in the same MLT sector - where one patch could have just started its journey across the polar cap while another is halfway across - could be at completely different phases; one not yet affected by the gradient drift instability and the other showing very complex plasma density structures forming in its trailing edge.

Due to the Dungey cycle resulting in anti-sunward drift of polar cap patches across the polar regions, we expect to observe that the gradient drift instability has permeated through more of the polar cap patches located on the nightside. Resulting in a bigger share of polar cap patches categorized as being affected by GDI (green bar).

This agrees well with the f-ratios in the nightside magnetic local time sectors (MLT $21 - 24$ and $0 - 03$) in figure 4.7. Both hemispheres show that there are more polar cap patches affected by the gradient drift instability than not, except for MLT $0 - 03$ in the northern hemisphere (although the difference is not as big as for dayside MLT sectors).

Additionally, the results from the dusk/dawn sectors, presented in figure 4.8, behave in accordance with the aforementioned theoretical aspects. Gradient drift instability determination on the dayside suggests that the majority of polar cap patches have not been sufficiently affected, even though a large number of patches exhibit gradient drift instability occurrence. Polar cap patches situated on the nightside (MLT $18 - 21$ and $3 - 6$) suggest that the greater share of patches have a large contrast with respect to trailing and leading edge plasma density structures, i.e. high f-ratios. This further strengthens the underlying hypothesis that the trailing edge of polar cap patches provide suitable conditions and is susceptible to the gradient drift instability.

As previously mentioned over 8 thousand polar cap patches have been located and used in the polar cap patch gradient drift instability and climatology study. When working with and analyzing the data produced in this master project it is clear to see that there is an unequal amount of polar cap patches located on the Earth's dayside and nightside. More precisely, there are 4808 polar cap patches on the dayside and 3284 polar cap patches on the nightside. This could come as a result of multiple factors, some of them being slow diffusion of the polar cap patches due to collisions in the ionosphere, turbulence or the presence different fluid and plasma instabilities. Nonetheless, it is possible that this is a result of the gradient drift instability. In theory, the polar cap patches are continuously affected by the gradient drift instability as they drift across the polar cap regions. GDI could dissolve the polar cap patches torn from the high density plasma located on the dayside before they are able to cross over to the Earth's nightside.

5.2 Polar Cap Patch Climatology Study

Now that we have discussed whether the polar cap patches are susceptible to the gradient drift instability, which may result in signal degrading through scintillation, we can further examine when PCPs are expected to pose a greater threat to GNSS signal quality.

Figure 4.9 shows that the polar cap patches used in this master project were identified by Swarm A and Swarm C. No patches where located by Swarm B. This is most likely due to the fact that Swarm B orbits the Earth at a different altitude when compared to Swarm A and Swarm C.

The expected occurrence rate of polar cap patches is strongly linked to the offset of the Earth's rotational axis and the orientation of its magnetic field with respect to the plane of the Earth's orbital plane. Henceforth using the northern hemisphere as an example. The polar cap is mostly pointed away from the Sun during local winter conditions. This results in a notable difference between the dayside ionospheric plasma, created through photoionization as discussed in chapter 2, and the low density ionospheric plasma on the nightside.

However, this is not the case when considering local summer conditions. During local summer, the high energy radiation from the Sun mostly covers the polar cap and is therefore able to ionize the neutral gas in the region. Making it much more difficult to obtain density enhancement of at least twice that of the background density, which is the characteristic density of a polar cap patch.

Figure 4.9 shows the occurrence rate of polar cap patches in the northern and southern hemisphere. Blue and yellow background colors indicate local winter and local summer conditions in the hemispheres. The polar cap patch occurrence rate display a clear tendency towards being higher during local winter conditions with respect to the northern hemisphere. This is also the case when considering the polar cap patch occurrence in the southern hemisphere. The polar cap patch occurrence rate is at its highest during local winter conditions in the southern hemisphere, although the results are not as unambiguous.

The results shown in figure 4.9 coincide well with the expected occurrence rate deduced from the underlying physics principles. Polar cap patches display a notably higher occurrence rate during local winter conditions. Thus, further suggesting that scintillations due to complex density structures in polar cap patches pose a greater threat to GNSS signals passing through the ionosphere during local winter conditions.

5.2.1 Correlation with Other Studies

Other studies of the interhemispheric polar cap patch occurrence rate have been done by Chartier et al. and Spicher et al. (Chartier et al. 2018; Spicher et al. 2017). Chartier et al. found polar cap patches to occur more frequently around December for both hemispheres. In other words, during local winter and local summer for the northern and southern hemisphere, respectively. This contradicted the findings of Spicher et al.. Spicher et al. found the occurrence rate of polar cap patches to be notably higher during local winter for both the northern and southern hemisphere.

A strong correlation with Spicher et al.'s findings can be found when comparing my polar cap patch climatology study with previously done studies. This may very well be due to the fact that both studies utilize the same Polar Cap Patch Detection Algorithm

(PCPDA) (Clausen et al. 2017). Nevertheless, this project's and Spicher et al.'s polar cap patch occurrence rate study span over different time periods and use different Swarm data products. The fact that the studies achieve similar results can still provide some sort of additional strength to the hypothesis that the polar cap patch occurrence rate favours local winter conditions.

5.3 Methodology

Different approaches to this master project's methodology will be discussed in the following section. It will be primarily focused on the polar cap patch gradient drift instability study. The polar cap patch gradient drift study uses the IPIR Swarm data product (Jin et al. 2022) to locate polar cap patches before comparing plasma density structures in their trailing and leading edge.

The initial aim of this master project was to download and analyze in situ measurements made by the Swarm satellite constellation from mid 2014 up until the beginning of 2023. A total time span of approximately 8.5 years. However, this did not go according to plan due to errors related to the MLAT and MLT data conversion. The working theory is that there is a problem in the implementation of the International Geomagnetic Reference Field (IGRF) in the Python wrapper ApexPy. Eventually, after numerous attempts to locally implement the correct IGRF version into the ApexPy software, it was decided that the best approach was to shorten the study's time frame to mid 2014 to the end of 2019. A 5.5 years time period. It was possible to use an older IGRF version, however this would only provide inaccurate estimates of the MLT and MLAT data - which was not desirable.

The trailing and leading edge of the polar cap patches were determined by comparing the MLAT value of the PCP start and end in addition to where the measurements where situated with respect to MLT sectors. This could lead to some inaccurate edge definitions. Especially in the regions where the satellite trajectories go from dusk to dawn or vice versa. A more advantageous approach could be to first determine the actual satellite trajectory of the individual polar cap passes in a MLT coordinate system and find its angle with respect to the line between MLT noon-midnight. This could then be used to determine the trailing and leading edge of polar cap patches along the trajectories. Yet, I believe that this would only apply to an insignificant amount of polar cap patches and therefore be of little importance to the overall results of the GDI study.

Furthermore, an assumption made in the method used to identify the trailing and leading edge in polar cap patches is that the PCPs follow strict anti-sunward trajectories across the polar cap regions. In other words, the polar cap patches only drift in straight lines across the polar regions from the dayside to the nightside. However, this is not always the case. A study conducted by Oksavik et al. 2010, demonstrated that the simplified image of anti-sunward flow had to be adjusted. Oksavik et al. found that the flow direction of polar cap patches is susceptible to change. Some PCPs can even rotate, resulting in the trailing edge becoming the leading edge and vice versa (Oksavik et al. 2010). A possible consequence of the PCP flow direction changes and rotation is inaccurate trailing and leading edge determination. As previously mentioned in the methodology chapter (3), the initial plan for this master project was to use ion drift measurements from the Thermal Ion Imagers. Ion drift measurements could identify each trailing and leading edge based on the PCP drift velocity, not only where the PCPs are situated in

the polar caps. This would have made it possible to determine the polar cap patch edges more accurately.

The results of the polar cap patch climatology study would not be affected by the somewhat inaccurate edge determination, given that we are only interested in when and where the polar cap patches occurred.

Another aspect to keep in mind is that it could be possible for the Swarm satellites to identify the same polar cap patch more than once, given that Swarm A and Swarm C orbit the Earth in close proximity to each other (*Swarm mission* 2023). Consequently, the satellites could pass through the same polar cap patch, but at different locations. This could, to some degree, affect the result in both the polar cap patch gradient drift instability study and climatology study. With respect to the gradient drift instability study, it could result in comparing the trailing and leading edge at multiple locations. Most likely, this would not affect the overall results of the study. It could however, provide a more accurate comparison of the edges in the polar cap patches that were passed twice.

The possible detection of the same polar cap patch could also have an effect on the polar cap patch occurrence rate study. Double satellite detection could inflate the number of daily occurrences in the climatology study. I believe that the resulting change in occurrence rate would be somewhat randomized - affecting the overall results to the same degree. Consequently, it can be argued that the local winter condition bias would remain unchanged.

Chapter 6

Conclusion and Future Outlook

6.1 Conclusion

The main objective of this master thesis was to investigate the occurrence of gradient drift instability in the trailing edge of polar cap patches. This was attempted through a quantitative study of in situ plasma density measurements taken by the Swarm satellites. 8092 polar cap patches and their respective trailing and leading edge have been determined using a combination of the preexisting PCP_flag data, and the generated magnetic local time and magnetic latitude data. Subsequently, the trailing and leading edge were compared using the standard deviation of a linear regression with respect to the plasma density. The results have been presented using statistical plots such as histograms and bar charts.

The main finding of the polar cap patch gradient drift instability study is that there is a significant difference in the occurrence of GDI in polar cap patches when comparing the Earth's dayside and nightside. The majority of nightside polar cap patches appear to be affected by the gradient drift instability, showing substantial differences in plasma density fluctuations in the trailing edge when compared to the leading edge. This is in agreement with the underlying physical characteristics of the gradient drift instability. Thus, supporting the hypothesis that the gradient drift instability affects polar cap patches drifting across the polar cap and that it predominantly acts on its trailing edge.

This master thesis' secondary objective was to examine the interhemispheric polar cap patch occurrence rate in order to quantify when to expect PCPs to pose a greater threat to GNSS signals. The PCP occurrence rate study was conducted using the same 8092 polar cap patches as the GDI study. The daily PCP occurrence number were divided by the hours spent by the satellite over the polar cap regions and subsequently plotted. As previously mentioned, studies conducted by Chartier et al. 2018 and Spicher et al. 2017 were in disagreement whether the polar cap patch occurrence rate is highest in December or during local winter conditions, respectively. The finding of this master thesis is that polar cap patches occur more frequently during local winter conditions. Thereby lending support to Spicher et al.'s conclusion, and reinforcing the current understanding of polar cap patch formation theory.

6.2 Future Outlook

This master thesis is the first quantitative polar cap patch study that examines the relation between polar cap patches and the gradient drift instability. Hopefully the methodology and results of this thesis can be used as an encouragement to conduct similar studies in the future. As previously discussed, it could be interesting to see whether another way of locating the trailing and leading edge of polar cap patches would yield corresponding results. Hopefully, the problems concerning the Thermal Ion Imagers can be solved. It would be particularly interesting to compare the findings of this master thesis with a similar study using ion drift velocity for determining the polar cap patch edges.

It could be beneficial to include additional parameters in the Ionospheric Plasma IRregularities data product, as it has shown to be very useful in this master thesis. Especially two parameters come to mind; magnetic latitude (MLAT) data and magnetic local time (MLT). Magnetic latitude and magnetic local time data is widely used in studies of different phenomenon in space physics due to its direct link to the dynamics of the Earth's magnetosphere. Additionally, this would work towards one of the secondary goals of IPIR as there are multiple ways to generate MLAT and MLT data - to provide a reference dataset that reduce contradicting results due to methodical inconsistencies (Jin et al. 2022).

Appendix A

The Python Code

The codes used in order to retrieve, process and analyze the Swarm data can be found on github: https://github.com/Kristofferto/Master-Project-Spring-2023

Bibliography

Acharya, R. (2015). *Understanding Satellite Navigation*. Academic Press.

Alken, P., E. Thébault and C.D. Beggan (2021). 'International Geomagnetic Reference Field: the thirteenth generation.' In: *Earth Planets Space* 73.49. DOI: https://doi.org/10.1186/s40623-020-01288-x.

Aon, E. F., R. Q. Shaddad, A. R. Othman and Y. H. Ho (2014). 'Analysis of ionospheric scintillation for global navigation satellite system at UTeM, Malaysia'. In: *2014 IEEE 10th International Colloquium on Signal Processing and its Applications*, pp. 37–41.

Bothmer, V. and I. A. Daglis (2007). *Space Weather - Physics and Effects*. Springer, New York.

Chartier, A. T., C. N. Mitchell and E. S. Miller (2018). 'Annual Occurrence Rates of Ionospheric Polar Cap Patches Observed Using Swarm'. In: *Journal of Geophysical Research: Space Physics* 123.3, pp. 2327–2335. DOI: https://doi.org/10.1002/2017JA024811.

Chen, F. F. (2016). 'Introduction to Plasma Physics and Controlled Fusion.' In: DOI: https://doi.org/10.1007/978-3-319-22309-4.

Clausen, L. B. N., W. J. Miloch and V. Lofstad (2017). *Swarm + Innovation, Polar Cap Products*. https://www.mn.uio.no/fysikk/english/research/projects/swarm/. Accessed: January 20.

Crowley, G. (1996). *Critical review of ionospheric patches and blobs*. Oxford University Press, pp. 619–648.

Dunbar, B. (2022). *The Heliopedia*. https://www.nasa.gov/mission_pages/sunearth/the-heliopedia. Accessed: March 29.

Dungey, J. W. (1961). 'Interplanetary Magnetic Field and the Auroral Zones'. In: *Phys. Rev. Lett.* 6 (2), pp. 47–48. DOI: 10.1103/PhysRevLett.6.47.

Emmert, J. T., A. D. Richmond and D. P. Drob (2010). 'A computationally compact representation of Magnetic-Apex and Quasi-Dipole coordinates with smooth base vectors'. In: *Journal of Geophysical Research: Space Physics* 115.A8. DOI: https://doi.org/10.1029/2010JA015326.

Gondarenko, N. A. and P. N. Guzdar (2004a). 'Density and electric field fluctuations associated with the gradient drift instability in the high-latitude ionosphere'. In: *Geophysical Research Letters* 31.11. DOI: https://doi.org/10.1029/2004GL019703.

Gondarenko, N. A. and P. N. Guzdar (2004b). 'Plasma patch structuring by the nonlinear evolution of the gradient drift instability in the high-latitude ionosphere'. In: *Journal of Geophysical Research: Space Physics* 109.A9. DOI: https://doi.org/10.1029/2004JA010504.

Gondarenko, N. A. and P. N. Guzdar (2006). 'Simulations of the scintillation-producing irregularities in high-latitude plasma patches'. In: *Geophysical Research Letters* 33.22. DOI: https://doi.org/10.1029/2006GL028033.

Hutchinson, I. H. (2002). *Principles of Plasma Diagnostics*. 2nd ed. Cambridge University Press. DOI: 10.1017/CBO9780511613630.006.

Jin, Y., D. Kotova, C. Xiong, S. M. Brask, L. B. N. Clausen, G. Kervalishvili, C. Stolle and W. J. Miloch (2022). 'Ionospheric Plasma IRregularities - IPIR - Data Product Based on Data From the Swarm Satellites'. In: *Journal of Geophysical Research: Space Physics* 127.4. DOI: https://doi.org/10.1029/2021JA030183.

Jin, Y., J. I. Moen and W. J. Miloch (2014). 'GPS scintillation effects associated with polar cap patches and substorm auroral activity: direct comparison'. In: *J. Space Weather Space Clim.* 4, A23. DOI: 10.1051/swsc/2014019.

Kelley, M. C. (1989). *The Earth's Ionosphere, Plasma Physics and Electrodynamics*. Academic Press.

Kelley, M. C. (2009). *The Earth's Ionosphere*. Academic Press.

Keskinen, M. J. and S. L. Ossakow (1983). 'Theories of high-latitude ionospheric irregularities: A review'. In: *Radio Science* 18.6, pp. 1077–1091. DOI: https://doi.org/10.1029/RS018i006p01077.

Kivelson, M. G. and C. T. Russell (1995). *Introduction to Space Physics*. Cambridge University Press.

Lockwood, M. and H. C. Carlson Jr. (1992). 'Production of polar cap electron density patches by transient magnetopause reconnection'. In: *Geophysical Research Letters* 19.17, pp. 1731–1734. DOI: https://doi.org/10.1029/92GL01993.

McPherron, R. L. (1995). 'Magnetospheric Dynamics'. In: *Introduction to Space Physics*. Ed. by M. R. Kivelson and C. T. Russell. Cambridge University Press. Chap. 13. ISBN: 9780521451048.

Meeren, C. van der, K. M. Laundal, A. G. Burrell, L. L. Lamarche, G. Starr, A. S. Reimer and A. Morschhauser (Apr. 2023). *aburrell/apexpy: ApexPy Version 2.0.1*. Version v2.0.1. DOI: 10.5281/zenodo.7818719.

Moen, J., K. Oksavik, L. Alfonsi, Y. Daabakk, V. Romano and L. Spogli (2013). 'Space weather challenges of the polar cap ionosphere.' In: *J. Space Weather Space Clim.* 3.A02.

Morley, S. K., J. Koller, D. T. Welling, B. A. Larsen, M. G. Henderson and J. T. Niehof (2011). 'Spacepy - A Python-based library of tools for the space sciences'. In: *Proceedings of the 9th Python in science conference (SciPy 2010)*. Austin, TX.

Oksavik, K., V. L. Barth, J. Moen and M. Lester (2010). 'On the entry and transit of high-density plasma across the polar cap'. In: *Journal of Geophysical Research: Space Physics* 115.A12. DOI: https://doi.org/10.1029/2010JA015817.

Parker spiral (2022). https://www.esa.int/ESA_Multimedia/Images/2019/03/Parker_spiral. Accessed: March 29.

Pécseli, H. L. (2020). *Waves and Oscillations in Plasmas*. CRC Press. DOI: https://doi.org/10.1201/9780429489976.

Petrovski, I. G. and T. Tsujii (2012). 'Electromagnetic scintillation of GNSS signal'. In: *Digital Satellite Navigation and Geophysics: A Practical Guide with GNSS Signal Simulator and Receiver Laboratory*. Cambridge University Press, pp. 241–269. DOI: 10.1017/CBO9780511659072.012.

Russel, C. T., J. G. Luhmann and R. J. Strangeway (2016). *Space Physics: An Introduction*. Cambridge University Press.

Spicher, A., T. Cameron, E. M. Grono, K. N. Yakymenko, S. C. Buchert, L. B. N. Clausen, D. J. Knudsen, K. A. McWilliams and J. I. Moen (2015). 'Observation of polar cap patches and calculation of gradient drift instability growth times: A

Swarm case study'. In: *Geophysical Research Letters* 42.2. DOI: https://doi.org/10.1002/2014GL062590.

Spicher, A., L. B. N. Clausen, W. J. Miloch, V. Lofstad, Y. Jin and J. I. Moen (2017). 'Interhemispheric study of polar cap patch occurrence based on Swarm in situ data'. In: *Journal of Geophysical Research: Space Physics* 122.3. DOI: https://doi.org/10.1002/2016JA023750.

Stix, M. (2012). *The Sun: An Introduction*. Springer Berlin, Heidelberg. DOI: https://doi.org/10.1007/978-3-642-56042-2.

Swarm Data Access (2023). https://swarm-diss.eo.esa.int/?fbclid=IwAR1hnbfnDjaj30Z3AbbUtv1RpC0z_Wo2GAjv9pVhZ8f5D0C4uLbB7C-awjo#swarm%2FLevel2daily%2FEntire_mission_data%2FIPD%2FIRR. Accessed: January 25.

Swarm mission (2023). https://earth.esa.int/eogateway/missions/swarm. Accessed: February 27.

Tsunoda, R. T. (1988). 'High-latitude F region irregularities: A review and synthesis'. In: *Reviews of Geophysics* 26.4, pp. 719–760. DOI: https://doi.org/10.1029/RG026i004p00719.

Virtanen, P., R. Gommers, T. E. Oliphant, M. Haberland, T. Reddy, D. Cournapeau, E. Burovski, P. Peterson, W. Weckesser, J. Bright, S. J. van der Walt, M. Brett, J. Wilson, K. J. Millman, N. Mayorov, A. R. J. Nelson, E. Jones, R. Kern, E. Larson, C J Carey, İ. Polat, Y. Feng, E. W. Moore, J. VanderPlas, D. Laxalde, J. Perktold, R. Cimrman, I. Henriksen, E. A. Quintero, C. R. Harris, A. M. Archibald, A. H. Ribeiro, F. Pedregosa, P. van Mulbregt and SciPy 1.0 Contributors (2020). 'SciPy 1.0: Fundamental Algorithms for Scientific Computing in Python'. In: *Nature Methods* 17, pp. 261–272. DOI: 10.1038/s41592-019-0686-2.

Weber, E. J., J. Buchau, J. G. Moore, J. R. Sharber, R. C. Livingston, J. D. Winningham and B. W. Reinisch (1984). 'F layer ionization patches in the polar cap'. In: *Journal of Geophysical Research: Space Physics* 89.A3, pp. 1683–1694. DOI: https://doi.org/10.1029/JA089iA03p01683.

Weber, E. J., J. A. Klobuchar, J. Buchau, H. C. Carlson Jr., R. C. Livingston, O. de la Beaujardiere, M. McCready, J. G. Moore and G. J. Bishop (1986). 'Polar cap F layer patches: Structure and dynamics'. In: *Journal of Geophysical Research: Space Physics* 91.A11, pp. 12121–12129. DOI: https://doi.org/10.1029/JA091iA11p12121.